8-2014

Hybrid Rocket Design Study Utilizing Nozzle Cooling and Aft-End Vortex Oxidizer Injection

John Nicholas Quigley
University of Tennessee - Knoxville, jquigle1@utk.edu

To the Graduate Council:

I am submitting herewith a thesis written by John Nicholas Quigley entitled "Hybrid Rocket Design Study Utilizing Nozzle Cooling and Aft-End Vortex Oxidizer Injection." I have examined the final electronic copy of this thesis for form and content and recommend that it be accepted in partial fulfillment of the requirements for the degree of Master of Science, with a major in Aerospace Engineering.

James E. Lyne, Major Professor

We have read this thesis and recommend its acceptance:

Kivanc Ekici, Zhili Zhang

Accepted for the Council:
Dixie L. Thompson

Vice Provost and Dean of the Graduate School

(Original signatures are on file with official student records.)

Hybrid Rocket Design Study Utilizing Nozzle Cooling and Aft-End Vortex Oxidizer Injection

A Thesis Presented for the
Master of Science
Degree
The University of Tennessee, Knoxville

John Nicholas Quigley
August 2014

ABSTRACT

The current study focused on two innovations intended to reduce the cost and enhance the performance of hybrid rockets. The majority of the emphasis was placed on the design, fabrication and testing of a 3-D printed, water cooled nozzle. This work was done as proof of concept to show that complex, high temperature components could be manufactured using these new techniques, thereby substantially bringing down fabrication costs and allowing configurations that are not feasible using traditional machining. A water-cooled calorimeter nozzle was made and used in thrust stand tests to verify analytic and numerical heating models used in the design of the nozzle. Agreement was good between the predicted and measured heating rates. This experimental work helped to validate the nozzle design approach which will now be used to devise a 3-D printed, regeneratively cooled nozzle for a hybrid engine. The secondary phase of the study was an analysis of aft-end vortex oxidizer injection as a means of enhancing fuel regression rates. Components are currently being fabricated as part of an ongoing study to compare engine performance results for traditional head end and aft-end vortex injection.

TABLE OF CONTENTS

List of Tables

List of Figures

List of Symbols

Symbols

A- cross sectional area
A^* - area ratio
A_c - cross sectional area
$A_{c\text{-}chamber}$ – cross sectional area of combustion chamber
AEVI- aft end vortex injection
C_f - skin friction coefficient
CR – engine contraction ratio - D_c/D_t
C_t - thrust coefficient
C_p – specific heat
C^* - characteristic velocity
D – diameter
D^* - throat diameter
G – mass flux, lbm/in^2
Nu-Nusselt number
H – enthalpy, mass specific
h - heat transfer coefficient
h_v- heat of vaporization
ID – inner diameter
L- length of fuel grain
M – Mach number
MW – molecular weight
$\dot{m}$ - mass flow rate
O/F- oxidizer to fuel ration
P_a – atmospheric pressure
P_c - combustion chamber pressure
P_e – exit plane pressure
P_0 – total pressure
Pr – Prandtl number
R- gas constant
Re – Reynolds number
$\dot{q}$- heat flux
St- Stanton number
r - radius
r^* - throat radius
$\dot{r}$ - regression rate/burn rate
r_c- axial radius of curvature at throat
t- thrust
T- temperature
T_{flame} – adiabatic flame temperature
$T_{fuel\ surface}$ – melting temperature of solid fuel
u- velocity
w_t- wall thickness

Acronyms

AEVI- Aft-end vortex injection
US - upper stage
GLOW - gross liftoff weight

Greek

Δ- difference
γ – ratio of specific heats
η – efficiency factor
δ- boundary layer thickness
ρ – density
ω – exponent of viscosity-temperature relation
μ – dynamic viscosity

Subscripts

c – combustion
e – boundary layer edge values
t -thrust
i – ideal
inj - injector
fg - fuel grain
fs- free stream
hg-hot gas side
ox - oxidizer
wh - hot wall
0 - stagnation/combustion chamber conditions

Chapter I
Introduction

A. Background

a. General

Hybrid rockets are characterized by those that combine a solid fuel grain with a liquid or gaseous oxidizer. During operation, the oxidizer is fed into the combustion chamber which is usually lined by the solid fuel grain. Here, the solid fuel will burn off and mix with the oxidizer as it reacts and exits through the nozzle. A diagram showing a typical hybrid rocket is shown below in Fig. 1.

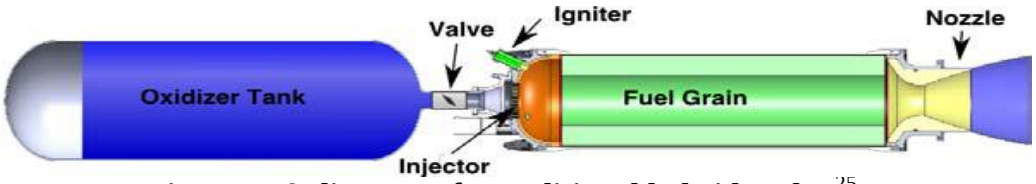

Figure 1: A diagram of a traditional hybrid rocket[25]

b. Motivation

The growing demand for smaller sized satellites, or nano-satellites, has turned attention towards smaller launch vehicles capable of placing relatively small payloads in orbit. As the cost is currently near 7 million dollars for any dedicated orbital launch mission,[3] the best option for nano-sats is to piggyback on larger missions with extra payload space, or for many smaller payloads to share a single launch vehicle. This either limits the entire payload to a single orbit or requires that each satellite have a separate upper stage motor for individual orbital insertion from the final launch condition. Being able to utilize an upper stage engine for a secondary payload on a rideshare is a significant request, as individual propulsion systems for the secondary payloads add weight and additional risk of damage to the primary payload. Hybrids bring a unique set of features into the picture that may render them useful as upper and lower stage rockets. More importantly, they may be able to utilize propellant combinations that reduce the threat to the primary payload, while being cheaper to produce. Ultimately, it is desired to develop a more economical method for delivering nano-sats to orbit.

c. A Sensible, Economical Rocket

In this study performance is secondary to durability, versatility, economy and safety. It is intended to achieve this with an ABS (Acrylonitrile Butadiene Styrene)/Nitrous Oxide hybrid rocket.

ABS was selected as the solid fuel due to its ready availability, favorable mechanical properties and price. Its favorable mechanical properties allow it to serve as its own pressure vessel, meaning heavy reinforcements won't be required. It can be 3-D printed, if so desired, or bought in cylindrical form and hollowed out to form the combustion chamber/fuel grain.

Nitrous Oxide is also readily available and is known to be relatively safe in stored form. N_2O has high saturation pressure, non-toxicity and good performance.[7] Nitrous Oxide will not need to be cryogenic to maintain a liquid state, and its self-pressurizing properties will eliminate the need for oxidizer pumps.

d. Performance benefits

Aside from the economical benefits of a hybrid, they are an area of interest for their many desirable qualities over the usual pure liquid or pure solid rockets. They are intended to display the best of both worlds. Hybrids have the start stop capabilities and thrust modulation of a liquid rocket, while requiring one less propellant tank and providing the volumetric efficiency and reduced complexity associated with solid rockets. In addition to their potential performance gains, hybrids are also attractive due to their relative ease of manufacture and benign propellant combinations[1]. It is expected that an economical hybrid rocket can be developed for use in various applications, but they are expected to fill a much needed niche for small payloads.

Despite the potential gains of a hybrid, the relatively undeveloped state of hybrid rocket technology leaves pure solid and liquid rockets as the preferred commercial options. The primary hybrid performance hurdles to be overcome are the poor regression rates of the solid fuel, combustion instabilities in larger rockets[2] and poor mixing of the liquid oxidizer and solid fuel in the combustion chamber. The two proposed innovations for hybrid rocket improvement are a 3-D printed, regeneratively cooled nozzle and aft-end vortex oxidizer injection (AEVI).

B. Proposed innovations

a. AEVI

The performance and efficiency of a hybrid rocket are highly dependent upon the regression rate of the solid fuel, directly affecting thrust, and the mixing of the fuel and oxidizer. In recent studies, it has been found that a rotational flow field in the combustion chamber along the solid fuel grain can realize a 2-6 fold increase in regression rate over the traditional head end oxidizer injection scheme[9], while also improving propellant mixing in the combustion chamber. Increased regression rates result in a higher total mass of the exhausting propellant and generate more thrust.

AEVI is an operational strategy showing promise for improved fuel regression rates, where the oxidizer is injected tangential to the inner fuel grain wall, resulting in a rotational flow field inside the combustion chamber surrounded by the fuel grain. The oxidizer would first spiral up the grain from the injection location, then turn around and spiral back away from the head end and out the nozzle. The vortex flow field would create a thinner boundary layer and increase the distance and time the oxidizer travels along the grain. It would also facilitate better mixing

between the oxidizer and the solid fuel that has melted off of the fuel wall and entered the combustion chamber flow. The thinner boundary layer would create an increased heat flux to the fuel grain, resulting in a higher regression rate, while the extra distance along the fuel grain traveled by the oxidizer would effectively increase the length without actually using a longer fuel grain. The extended time the propellants spend in the chamber, along with the increased mixing, would encourage complete combustion of the reactants before leaving the combustion chamber. The general scheme is shown below[6] in Fig. 2.

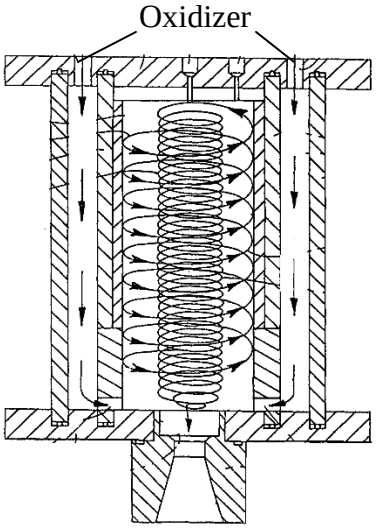

Figure 2 The aft-end vortex oxidizer injection scheme

Some preliminary findings for a rocket using this configuration are available from previous work[17], and an attempt to build on these was made in this study.

b. 3-D Printed, Regeneratively Cooled Nozzle

A regeneratively cooled nozzle design is intended to accomplish two things. First, the oxidizer will cool the nozzle walls, increasing the nozzle's ablation resistance. Second, the oxidizer is preheated before being injected into the combustion chamber, which has been shown to increase combustion stability[5]. By printing the cooling channels into the nozzle, it was expected that very thin walls may be realized, allowing for a much higher level of steady state heat flux between the hot gas side and the coolant side. Not only are the benefits of a regeneratively cooled rocket nozzle easier to implement with 3-D printing techniques, but the cooling concept becomes more effective with the channels actually printed into the nozzle itself.

A drawing of a regen cooled nozzle is shown below in Fig. 3b, while Fig. 3a shows a drawing of the two paired together.

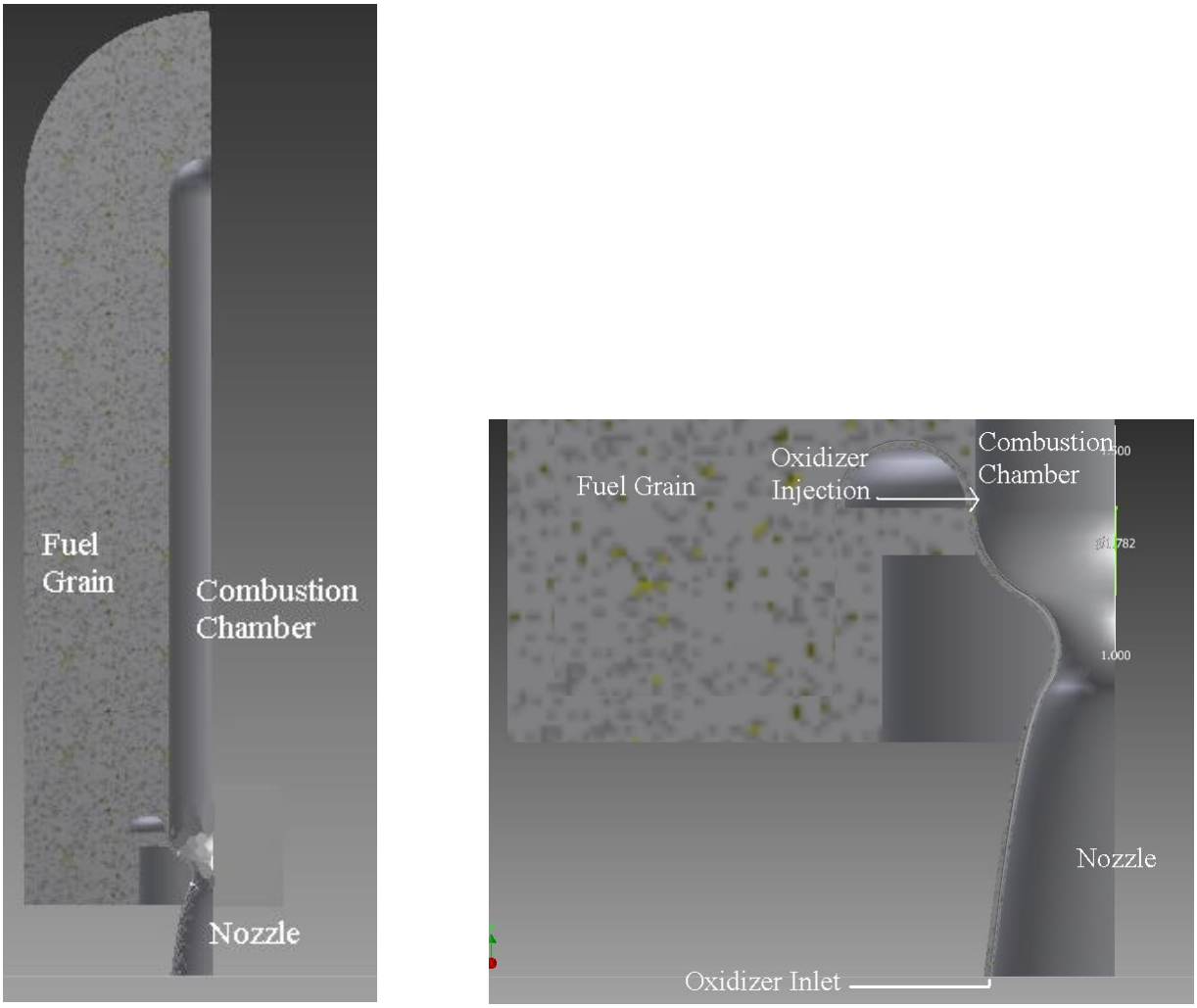

Drawn by Joseph Jones July 2009 [24]

Figure 3a,b The regen cooled nozzle scheme to be paired with AEVI

The ultimate goal is to combine these into a single flight weight vehicle, utilizing a regeneratively cooled nozzle that feeds the AEVI scheme in an effort to maximize performance, durability and economy. To our knowledge, these two innovations have never been combined on a rocket. An artist's rendition of this is shown above in Fig. 3a. By using 3-D printing technologies, it is expected to manufacture a single piece to serve as a regeneratively cooled nozzle with injectors. Aside from the oxidizer plumbing from the tank to the nozzle and the

ignition system, the primary rocket components could be manufactured in two pieces, requiring minimal assembly.

C. 3-D Printing via Selective Laser Melting, SLM

New manufacturing techniques, such as SLM (Selective Laser Melting)[8] which builds parts layer by layer in a 3-dimensional printer, allow the production of modestly sized complicated pieces out of a variety of materials and with essentially no labor. The complexity of the piece has no effect on the production costs, as it is typically a direct result of the size of the piece. An effort is currently underway to develop a flight weight rocket utilizing SLM, also known as rapid prototyping, in order to reduce the manufacturing difficulties associated with some of the more complex pieces. These pieces can be quickly produced and reproduced by the touch of a button. This decreases the manpower required for manufacturing and allows for much higher levels of complexity and repeatability to be achieved in the design. It is expected that by utilizing SLM, we will be able to consistently reproduce parts for testing, as well as for an eventual flight configuration.

D. Objectives

This work has been done to begin developing technology for the improvement of hybrid rockets by implementing regenerative cooling via a 3-D printed nozzle and an aft-end vortex oxidizer injection scheme.

a. 3-D printed, regeneratively cooled nozzle

A rocket nozzle that has the oxidizer running axially along the outside wall to cool the nozzle while preheating the oxidizer is not a new concept. The technology to 3-D print that nozzle, however, is new and the utilization of this technology has not yet been implemented to produce a 3-D printed, regeneratively cooled nozzle for a hybrid rocket. In a printed nozzle, the cooling channels can actually be printed inside of the nozzle walls.

An analytical/computational model was developed to generate expected thermal conditions and then validated with an experiment built around an Inconel-625, 3-D printed water cooled nozzle provided by NASA Marshall Space Flight Center.

Validated models and characterization of the operational responses are vital for the optimized design and dependable operation of such a piece. Minimum printing thicknesses are often greater than steady state wall thicknesses for typical heat loads on a cooled nozzle during operation. This requires some knowledge of the nozzle walls ablation response, if practical implementation of a 3-D printed, regeneratively cooled nozzle is to become a reality. During operation, it is unknown whether the hot nozzle wall surface would ablate away evenly while the cooler subsurface maintains its shape, or if the sub-surface material could possibly deform causing the nozzle to lose its shape and effectiveness. These issues are to be evaluated with

experiment. As this has never been done before, the experience is expected to provide necessary insights towards the flight implementation of such a piece.

If the nozzle can be printed and then slowly ablated to the required thickness, allowing for wall temperatures below the thermal limit, then we can potentially develop a 3-D printed regeneratively cooled nozzle capable of withstanding operational heat loads, resulting in a more durable and lightweight nozzle.

b. Aft-End Vortex Injection, AEVI

Hybrid rockets are known to have low solid fuel regression rates, resulting in a fairly high O/F ratio. Because of this, optimum O/F ratios cannot always be achieved without a long, heavy fuel grain, resulting in decreased volumetric efficiency.

In an effort to increase the regression rate in a hybrid rocket without adding weight, AEVI was evaluated for performance enhancement and mass savings versus the traditional injection methods for the same propellant combinations.

Experimentally developed, empirical regression rate relationships are the usual method for developing a regression rate relationship for a specific propellant combination and engine geometry. These are very specific to the operating conditions of the experiment from which the relation was produced. A model for the traditional head end injection that accounts for different propellant combinations has been developed[10] previously, but it is only valid for straight, head end injection. An empirical model for the AEVI scheme, also previously developed experimentally[15], was presented and modifications to account for different propellant combinations were proposed. A more universal model accurately predicting the regression rates resulting from an AEVI scheme would allow for a design to be optimized for greater ranges of flow rates, geometries and propellant combinations, while easing the need for expensive experimental studies. This could greatly reduce developmental costs for mission tailored, hybrid rockets.

Chapter II.
Rocket Model and Aft-End Vortex Performance Enhancement

Before the various design components are to be presented, the rocket model used for their implementation will be presented in this chapter. The basic rocket design methods will be presented, as well as the tools utilized for design.

A. Preliminary Analysis

a. Performance coefficients

In order to establish a performance baseline, a relatively traditional hybrid rocket model using validated techniques was established. ABS was the solid fuel and Nitrous Oxide was the oxidizer assumed in this analysis.

The performance coefficients C_t and C^* which represent thrust coefficient and characteristic velocity respectively, are shown below as their ideal values[2], first as functions of γ, P_0, P_e, P_a ,T_0, MW and A^*.

$$C_{t_i} = \sqrt{2 \times \gamma^2 \Big/ (\gamma - 1) \times (2/(\gamma+1))^{\gamma+1/\gamma-1} \times (1 - {P_e}/{P_0})^{\gamma-1/\gamma}} + \frac{P_e - P_a}{P_0} \times A^* \qquad (1)$$

$$C_i^* = \sqrt{1/\gamma \left(\frac{\gamma+1}{2}\right)^{\gamma+1/\gamma-1} \frac{\bar{R}}{MW} T_0} \qquad (2)$$

The ideal coefficients in Eqs. (1) and (2) can be related to rocket operating conditions and performance as shown in Eqs. (3) and (4) below[2].

$$P_0 = \eta_c C^*_{ideal} \dot{m} / A^* \qquad (3)$$

$$t = \eta_t C_{t_{ideal}} P_c A^* \qquad (4)$$

With these relations in mind, it is reasonable to begin analysis from the initial mixing of fuel and oxidizer in the combustion chamber. This allows for the evaluation of the gas properties used in Eqs. (1) and (2). The oxidizer mass flow was controlled, leaving the O/F ratio determined as a function of the solid fuel burn rate and the oxidizer flow rate.

b. Solid Fuel Regression Rate Model

The solid fuel in the combustion flow is a result of the regression rate, $\dot{r}$ and the surface area of the fuel grain. The regression rate model employs an enthalpy balance formulation taken from [8] resulting in Eq. 5 below.

$$\dot{r} = \frac{0.047}{\mathrm{Pr}^{0.1532} * \rho_{fuel}} \times \left[\frac{C_p \left(T_{flame} - T_{fuelsurface} \right)}{h_v solidfuel} \right]^{0.23} \times \left(\frac{\dot{m}_{ox}}{A_{c-chamber}} \right)^{4/5} \times \left(\frac{\mu}{L} \right)^{1/5} \qquad (5)$$

In Eq. 5: Pr-Prandtl number, C_p- gas specific heat, μ-absolute viscosity, h_v- heat of vaporization of solid fuel, L- length of the fuel grain.

This model is highly preferred over the empirical regression rate relationships that would be developed experimentally with a curve fit to the results. The empirical relationships are only valid for a small range of engine geometries and oxidizer flow rates from which the original experiment was performed. The development of the regression rate model of Eq. 5 was done by Whitmore in [10], and the highlights are presented in the following discussion.

The heat flux is first related to the regression rate and the convective heat transfer in Eq. 6.

$$\mathrm{h}(\mathrm{T_{flame}} - \mathrm{T_{fuelsurface}}) = \dot{\mathrm{q}} = \rho_{\mathrm{solidfuel}} \dot{\mathrm{r}} \mathrm{h_v} \qquad (6)$$

The heat transfer coefficient is then related to the Stanton number as a function of the Prandtl number and wall skin friction coefficient as shown in Eqs. 7a,b[11]. Eq. 7b is formulated for laminar flow over a flat plate using Reynolds analogy,[11] relating heat transfer through a boundary layer to the local skin friction. The subscript e denotes boundary layer edge values.

$$h = C_p \rho_e u_e St \qquad (7a)$$

$$St = \frac{C_f}{2} Pr^{-2/3} \qquad (7b)$$

That concludes the presentation of the work done in Ref. 10 and a modification to this work is proposed below. While Eq. 7b is accurate for laminar or turbulent flow with Pr near 1, Pr will be closer to 0 .7, and Eq. 8, shown below, is valid for Pr closer to the expected range [11].

$$St = c_f/2 \left(1 + 13 \left(Pr^{2/3} - 1 \right) {c_f}/{2}^{1/2} \right)^{-1} \qquad (8)$$

An averaged skin friction relation as a result of the integrated local skin friction is presented[10] and reposted below in Eq. 9a, along with the correction factor in Eq. 9b to account for wall blowing effects associated with the solid fuel melting off the fuel wall and entering the flow field. Specific heat in Eq. 9b is that of the gas.

$$c_f = \frac{0.074}{Re^{1/5}} \qquad (9a)$$

$$c_{fb} = 1.27 \frac{Cp(T_f - T_{sf})}{h_v} c_f \qquad (9b)$$

The resulting modified enthalpy balance regression rate model is shown below in Eq 10. The modification in Eq. 10 came from the substitution of Eq. 8 for 7b in the approximation of the Stanton number used to develop Eq. 5.

$$\dot{r} = \frac{0.047}{B}\frac{(\rho_e u_e)^{4/5}}{\rho_f}\left(\frac{C_p(T_{flame}-T_{fuel\,surface})}{h_v}\right)^{0.23}\left(\frac{\mu}{L}\right)^{0.2} \qquad (10)$$

where

$$B = 1 + 13\left(Pr^{2/3} - 1\right)\left[\frac{0.047}{Re^{0.2}}\left(\frac{C_p(T_{flame}-T_{fuel\,surface})}{h_v}\right)^{-0.77}\right]^{0.5}$$

In order to implement this model, free stream flow conditions such as density and velocity are now additional requirements for evaluation of the solid fuel regression rate. To accomplish this, a substitution of oxidizer mass flow rate divided by the combustion chamber cross sectional area for the necessary free stream values will be made, as shown in Eqs. 11a-b.

$$\rho_e u_e = \dot{m}_{ox}/A_c \qquad (11a)$$

$$Re = \dot{m}_{ox} L_{grain}/A_c \mu \qquad (11b)$$

The final result is now displayed in Eq. 12 with no additional parameters required for solution. The only benefit of the modification is the St approximation made in Eq. 8 being better suited than the approximation made in Eq. 7b for Pr nearer the actual conditions. This alteration has resulted in a 20% effect on regression rate and little effect on overall rocket performance.

$$\dot{r} = \frac{0.047}{B}\frac{\left(\dot{m}_{ox}/A_c\right)^{4/5}}{\rho_{fuelgrain}}\left(\frac{C_p(T_{flame}-T_{fuel\,surface})}{h_v}\right)^{0.23}\left(\frac{\mu}{L}\right)^{0.2} \qquad (12)$$

where

$$B = 1 + 13\left(Pr^{2/3} - 1\right)\left[\frac{0.047}{\left(\dot{m}_{ox}\,L/\mu\,A_c\right)^{0.2}}\left(\frac{C_p(T_{flame}-T_{fuel\,surface})}{h_v}\right)^{-0.77}\right]^{0.5}$$

Flow properties, Pr, T_{flame} and μ, are determined from CEA[27] , Chemical Equilibrium with Applications, which is a chemical equilibrium code, assuming equilibrium reaction for the

given pressure and O/F ratio. The rest of the values are known from the rocket geometry and solid fuel properties. A complete mixing of solid fuel and liquid oxidizer is assumed for these calculations, and a uniform concentration is assumed throughout the B.L. The portion of the boundary layer immediately adjacent to the wall will be a fuel rich zone containing the flame zone. The outer layer will be mostly oxidizer/combustion products. This is illustrated in Fig. 4 below.

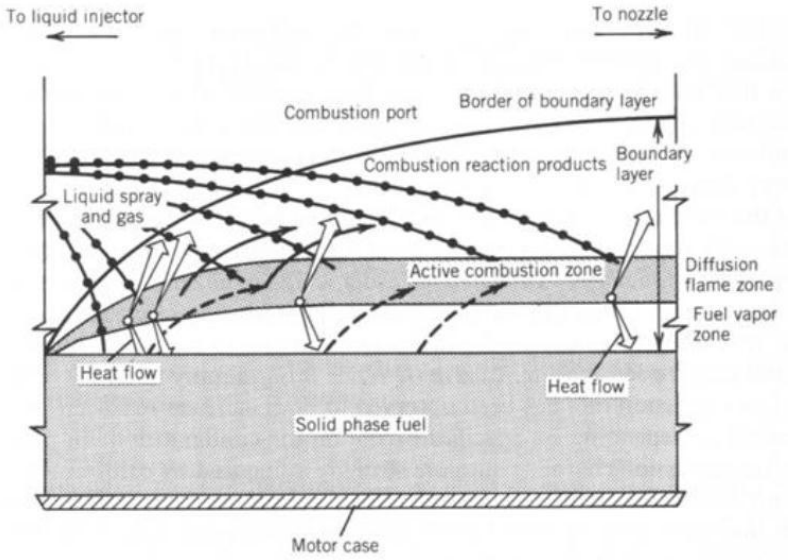

Figure 4 The boundary layer along the solid fuel grain in a hybrid rocket combustion chamber [26]

At startup, these flow properties would be ignition source dependent, requiring alterations for different ignition methods. In an effort to simplify the initial condition, the burn rate at the first time step is calculated using an empirical relation, experimentally developed for HTPB and Nitrous[12] shown as equation 11 below. HTPB has been shown to have similar characteristics to ABS[13]. This empirical relation predicts $\dot{r}$ as a function of G_{ox} only. Eq. 13 is in units of mm/s.

$$\dot{r} = 0.417 G_{ox}^{0.347} \qquad (13)$$

It is expected that these empirical relationships are not particularly accurate for a variety of rockets, as the relation in Eq 13 would be conditionally specific on geometry, range of oxidizer mass flux, etc. This is usually stated with the publication of the relationship. Hence, the empirical relation is only to be used as an initial condition.

c. Initial Performance Evaluation

The burn rate calculation paired with grain surface area provide a fuel flow rate and, hence, the O/F ratio is known. A chemical equilibrium code provided chamber conditions as well

as combustion gas properties and characteristic velocity (C^*) to be used in finding $C_{t\text{-}ideal}$ and the proceeding burn rate calculation using Eq 5. From these, along with Eqs. (3) and (4), the performance parameters are evaluated. The combustion efficiency (η_c) was assumed from previous work as 0.85 for theoretical values[14]. The nozzle efficiency (η_t) was assumed to be 0.9. This process would continue, in specified time steps, for the duration of the burn.

A baseline analytical model for a traditional head-end injection, ABS-Nitrous Oxide hybrid rocket has been developed. This was then modified to show the effects of an aft-end vortex injection scheme which was compared to the original. As an advantage of implementing aft-end vortex injection, η_c was arbitrarily increased from 0.85 to 0.93 in order to show the advantages and the regression rate was tripled. The regression rate increase is assumed conservative when compared to previous studies of a vortex flow field in the combustion chamber versus traditional oxidizer injection methods[9,15]. The results of the two analytical studies for identical rocket geometries and oxidizer injection are shown below in Figs. 5-9. The rocket's geometry is tabulated below in table 1. The results presented below were the result of the in house code (Appendix C) generated for this purpose.

Table 1: Rocket Nozzle and Fuel grain geometries, $\dot{m}_{ox}$=0.5 lbm/s

r^*, in	A/A^*	L , in	$ID_{fuel\ grain}$, in	$OD_{fuel\ grain}$, in
0.3	20	8	0.8	5

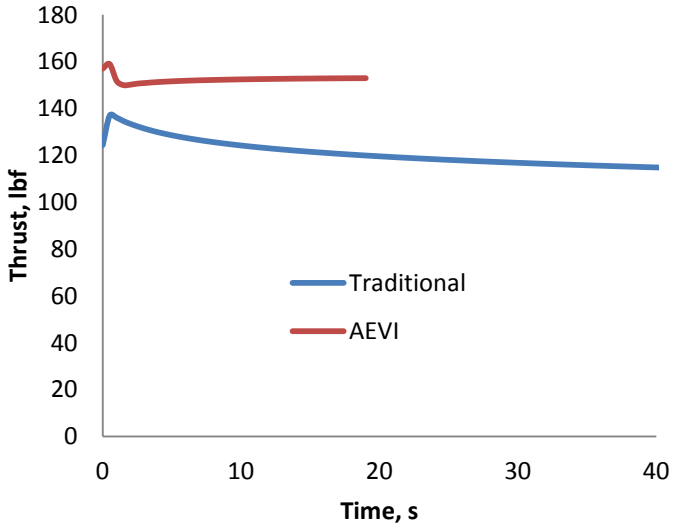

Figure 5. Thrust profiles for the traditional injection scheme along with the proposed aft-end vortex injection scheme (AEVI)
$\dot{r}_{a-e\ vortex} = 3\dot{r}_{traditional}$ and C^*_η=0.93 as opposed to C^*_η=0.85.

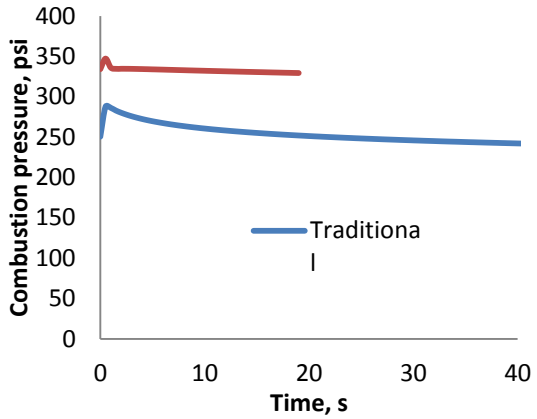

Figure 6. Comparison of combustion pressure

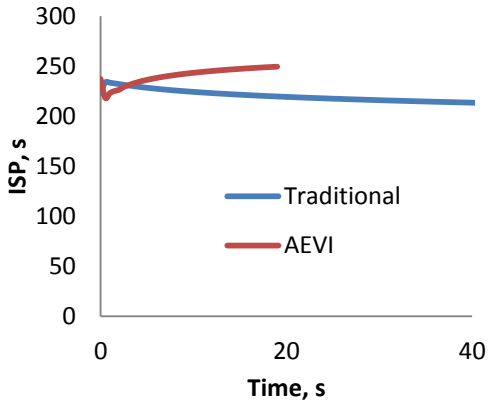

Figure 7 Specific Impulse Comparison

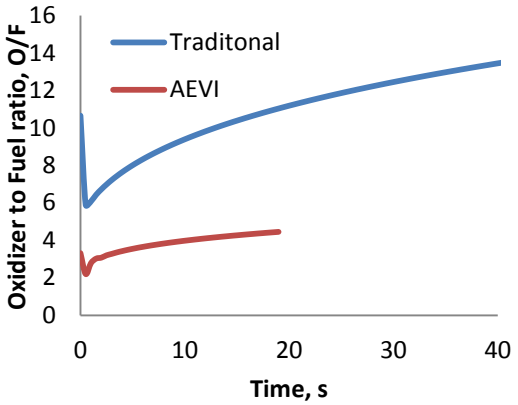

Figure 8 O/F ratios during operation.

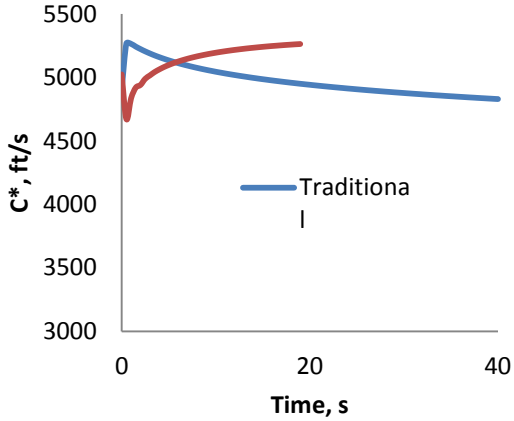

Figure 9 C^* comparison

Upon inspection of Figs. 5-9 the benefits of AEVI are fairly obvious without any effort towards optimization for the specified injection scheme. By observing the O/F plot in Fig.8, it would appear that the particular oxidizer flow rate and engine geometry were optimized for the traditional, head-end injection method. Optimal O/F is 7.5 for N_2O. The loss in performance over time for the traditional is due to the decrease in G_{ox}. The vortex injection is less dependent on G_{ox}, allowing for the increased burn area to have more effect than the loss of G_{ox} on rocket performance. For a specified wall thickness, the burn time is much shorter for the AEVI scheme. This would be expected with the resulting increased regression rate.

Operating conditions resulting from the study along with pertinent parameters are shown and compared in table 2. The improvements associated with AEVI are the result of increased mixing in the combustion chamber improving C^*_{η} and the increased total mass flow rate due to the higher solid fuel burn rate. Thrust levels from the simulation are what you would expect for

an upper stage rocket, and AEVI has shown to outperform the traditional injection scheme with no effort toward design optimization.

Table 2: Results for the traditional and aft-end vortex oxidizer injection comparisons

	$\dot{m}_{N2O}$, lbm/s	r^* ,in	P_c , psi	O/F	Thrust , lbs	C^* , ft/s	ISP , s
$\dot{r}_{traditional}$	0.5	0.3	256.1	5.9-12.7	119.3	4983.9	226.1
$\dot{r}_{a\text{-}e\ vortex}$	0.5	0.3	333.5	2.7-4.0	148.9	5075.7	247.5
Increase, %	n/a	n/a	30.2	n/a	24.8	1.8	9.5

After examining the results above, one can see the advantages to be gained from the flow field modification via AEVI and the usefulness of another study with adjusted rocket geometries and oxidizer flow rates.

B. AEVI Optimization

a. Setup

In Figs. 5-9, it was shown that a shorter fuel grain or a lower oxidizer flow rate should be utilized to exhibit a higher O/F ratio that would be closer to the optimal value of 7.5. The value in an experimental AEVI study can be clearly seen here as a means to accurately qualify the effects from the modified flow field due to the rotational oxidizer injection. The rocket geometry is modified for AEVI and specified below in table 3 and compared to the previous results for the traditional injection scheme. An O/F ratio of 7.5 is desired so the rocket parameters were specified in order to operate near this value.

Table 3: Rocket Nozzle and Fuel grain geometries, $\dot{m}_{ox}$=0.45 lbm/s

r^*, in	A/A^*	L , in	$ID_{fuel\ grain}$, in	$OD_{fuel\ grain}$, in
0.3	20	4	1.5	5

b. Results

Table 4: Geometry and Mass Comparisons Traditional vs AEVI

Dimension	Traditional	AEVI optimized
Length, in	10	4
ID, in	0.8	1.5
OD, in	3.2	5
Fuel grain mass , lbm	2.83	2.69
Oxidizer mass, lbm (25 sec runtime)	12.5	11.25
Total Mass, lb	15.33	13.94
Avg. Specific Impulse, s	228.3	253.2
Total Impulse, lb-s (25 second runtime)	5783.9	5877.3

Shown in table 4 above, is the mass savings in terms of fuel and oxidizer alone for the AEVI and traditional injection schemes. The total/specific impulse comparison shows a lighter and higher performing AEVI scheme. The weight advantage of the AEVI comes primarily from the decrease in oxidizer. This weight advantage will be increased by the reduction in necessary structural components for the shorter fuel grain, smaller oxidizer tank, etc. Figs. 5-9 are repeated below as Figs. 10a-e for further comparison of the different grain geometries and injections. The AEVI exhibits less degradation during the burn than does the straight head end injection allowing for a longer duration of sustained thrust.

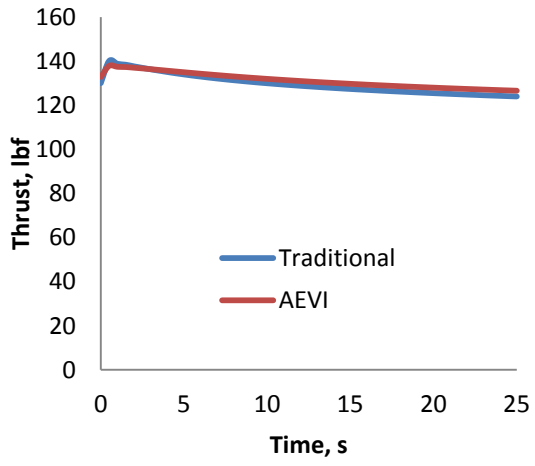

a. Thrust

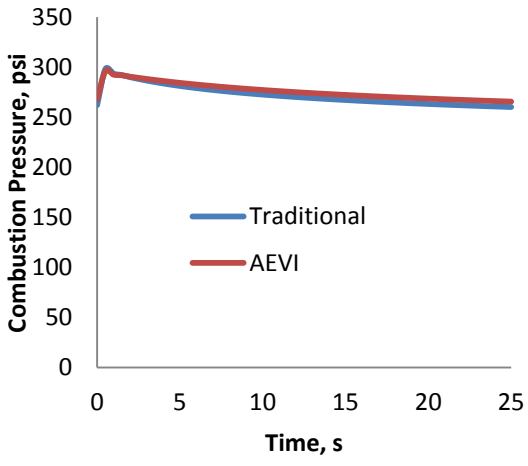

b. Pressure

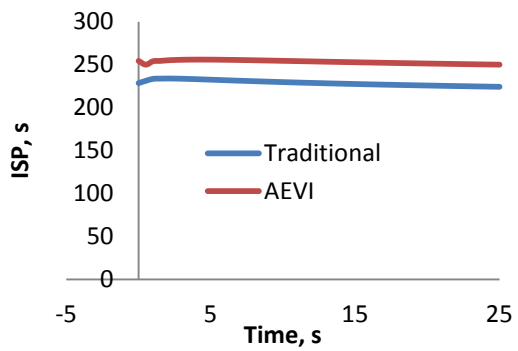

c. ISP

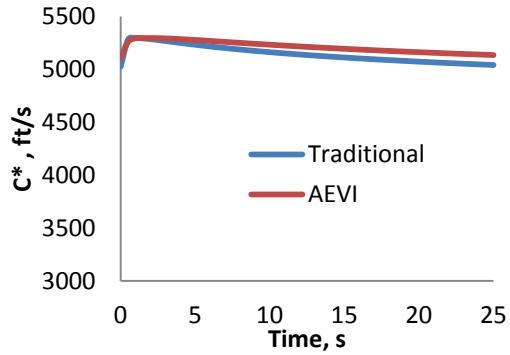

d. Cstar

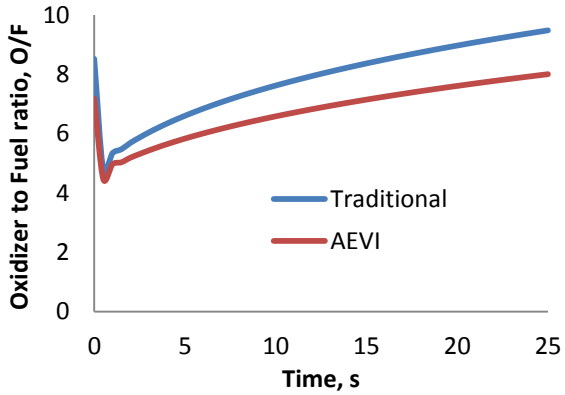

e. O/F ratio

Figure 10 a-e AEVI vs Head-End Performance Plots

C. Current AEVI Regression Rate Analytical Tools and Outlook

The AEVI regression rate method used in section B was a conservative and simplified model that allowed for a quick comparison to straight, head end injection rocket performance. In order to produce accurate results for a true design study, an accurate model characterizing AEVI was required. An effort to do this was initiated and pathways towards a more universal AEVI model were identified.

a. Status

Much of the preliminary work has been done on the Vortex injection scheme utilizing HTPB/PMMA for the solid fuel, instead of ABS and gaseous oxygen as the oxidizer[16,17,18], in order to accumulate data and gain experience with this scheme and its dependencies. Reference 17 concludes the following, with respect to an aft end vortex injection:

- Up to 640% increase in regression rates over the traditional injection scheme
- Fuel grain/combustion chamber ID had a significant effect on the regression rate as larger ID correlated to improved $\dot{r}$

- Local regression rate profiles consisted of three regimes: greatest sustained $\dot{r}$ at the injection end, decreasing $\dot{r}$ in the middle, and lower sustained $\dot{r}$ at the head end
- Injector mass flux and contraction ratio are also important parameters affecting ṙ[11]

The study in [17] was conducted for L/D ranging from 1.5-2.7 and port inner diameters as large as 5.08 cm. It is anticipated that the improvements on η_c and regression rate specified in the simulation above for this paper will be shown to be conservative as evidenced in references [16] and [17].

The positive effect of a larger inner diameter is a result of the corresponding increase in angular momentum. For no change in injector size or number and a constant mass flow rate, the oxidizer will be injected at the same velocity but at a greater distance from the axis of rotation[17].

The third regime of the regression rate profiles mentioned are said to be a result of a recirculation zone at the head end of the combustion chamber. As these tests were done for small L/D, a study on an extended or lengthened fuel grain may provide some insights to the point at which this three regime regression rate model will break down. An alternative empirical regression rate relationship accounting for the geometric parameters CR, L/D, G_{inj} and G_{ox} was developed[15] and is shown here in Eq. 14.

$$\dot{r} = 0.0085 CR^{0.45} (L/D)^{-0.59} {G_{inj}}^{0.45} {G_{ox}}^{0.37} \qquad (14)$$

For the two engines used to experimentally validate this relationship, an R^2 value of 0.977 was achieved with almost all of the data falling within ten percent of the predicted value. An even further improvement on this relationship was made in [11], utilizing a non-dimensional version of Eq. 14 with $R^2 = 0.992$ shown in Eq. 15.

$$\frac{\rho_f \dot{r}}{G} = 0.082 {Re_D}^{-.33} \left(\frac{St_{sw}}{St_0}\right) \left(\frac{St_v}{St_{sw}}\right) B \qquad (15)$$

B in Eq. 15 represents the blowing parameter and is detailed in reference 15. The methods for finding the Stanton number ratios are also presented, but are not given here.

It seems that a logical modification to Eqs. (14) and (15) for different fuel and oxidizer combinations would be via the Pr number. By altering the constants in 14 and 15 in accordance with mixture properties such as Pr, μ, C_p, density and enthalpy of vaporization of the solid fuel, to which the regression rate is related, it is expected to be able to accurately alter the constants in 14 and 15 to account for different propellant combinations. The weighting of each would need to be determined.

b. Outlook

The empirical regression rate relations are growing in number, as studies are being conducted for specific propellant and fuel grain geometry/injector combinations. However, models accounting for propellant combination, engine geometry and rocket size are not being

developed, at least not to the knowledge of this author. This would prove useful in decreasing the need for experimental studies required for evaluating specific hybrid motor configurations. An attractive avenue for this may be the combination of the studies presented thus far, covering enthalpy balance regression rate models and the growing knowledge of regression rate dependencies on various motor variables, resulting from the empirical regression rate studies paired with the non-dimensional regression rate analysis. By accounting for the effect of the centrifugal force on the skin friction coefficient, namely the spatial derivative term affecting the shear stress and in turn the skin friction, the vortex Stanton number, St_v, could be accounted for via Eq. 8 or some similar relation for the vortex flow field parameters. Perhaps a CFD model would allow for an accurate representation of this, without having to analytically define the spatial gradient providing the wall shear stress term.

Chapter III
Nozzle Heat Flux Investigation

This chapter focuses on the heat loads imposed on a cooled rocket nozzle and the wall temperature profiles for similar operating conditions to the model presented in chapter II. It is intended to compare these predictions to subsequent experimental data and by gaining confidence in our model, it can be used to design a regeneratively cooled nozzle with a reasonable expectation of success.

An analytical approach was first taken towards evaluating the expected heat loads and the resulting wall temperature profile. This was followed with the explanation of the experimental setup and the expected experimental thermal loads. The results of the experiment are in chapter IV.

A. Heat Flux Predictions

Predicted heat fluxes from a closed form approximation are presented here and were used as a foundation for the experimental design.

a. Closed Form approximation of heat transfer coefficient, Bartz's Method

In the interest of a less demanding heat flux prediction than is typically associated with CFD solutions, a correlation for the heat transfer coefficient, h, is shown below in Eq. 20[19]. A rapid estimation of the heat transfer coefficient could then be correlated to convective heat flux, $\dot{q}$, as shown in Eq. 21[12].

$$h_{hg} = \left[\frac{0.026}{(D^*)^2}\left(\frac{{\mu_o}^{0.2}c_p}{Pr^{0.6}}\right)_0\left(\frac{32.2P_0}{c^*}\right)^{0.8}\left(\frac{D^*}{r_c}\right)^{0.1}\right]\left(\frac{A^*}{A}\right)^{0.9}\sigma \tag{20a}$$

where

$$\sigma = \left[\left(\frac{1}{2}\frac{T_{wh}}{T_0}\left[1+\frac{\gamma-1}{2}M^2\right]+\frac{1}{2}\right)^{0.8-0.2\omega}\left(1+\frac{\gamma-1}{2}M^2\right)^{0.2\omega}\right]^{-1} \tag{20b}$$

$$\dot{q} = h_{hg}\left(T_{fs} - T_{wh}\right) \tag{21}$$

This particular relation requires only gas properties in the combustion chamber, which are determined with CEA, and the nozzle geometry. The only exception is that the free stream Mach number along the flow direction is required in Eq. 20b. The Mach number along the nozzle is evaluated with the isentropic mach number-area relationship and the free stream temperature, used in Eq. 21, is a function of the isentropic Mach number relationship. The heat flux is determined as shown in 21 using the hot-gas free stream temperature, T_{fs}, and T_{wh}. The hot side wall temperature is set at the designated ablation temperature of Inconel 625. This relation has

been developed by D.R. Bartz in [19,20] and shows an appropriate axial trend with a dependence on selecting the appropriate constant that corresponds to the appropriate boundary layer conditions at the throat. Results from Eqns. (20) and (21) are displayed below in Fig. 11 with nitrous oxide and ABS.

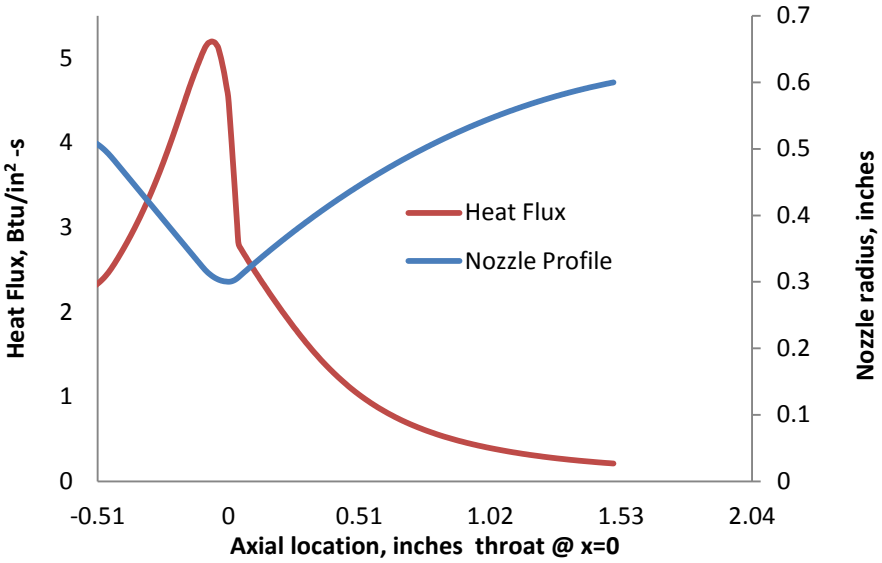

Figure 11. Analytical heat flux profile resulting from equation 20. Operational conditions: r*=0.3 in, O/F =6, P_c=305 psi

At the nozzle inlet, the heat transfer coefficient is underestimated but has been shown to yield accurate results at the throat[20]. The discontinuity in Fig. 11 is expected to be a result of the change in slope of the nozzle wall as the diverging section begins to straighten out. As a result the flow won't be accelerating as drastically, and the temperature drop will be affected, directly resulting in a change in the slope of the heat flux.

Some of the important details in [19] concerning Eq. 20 and its subsidiaries will be restated in the following discussion. First, the important assumptions made are as follows:

-no secondary flows due to combustion

- Aside from losses to the nozzle walls, T_0 is maintained

-no significant combustion instabilities

-chemical equilibrium conditions

- reversible flow outside the boundary layer

-fully turbulent boundary layer with constant specific heats and Pr in the B.L

-the boundary layer shape parameters are evaluated using a 1/7-power law

-heat transfer coefficient is primarily dependent upon local mass flux

-no changes in total enthalpy in the flow direction other than those caused by heat transfer to the wall

-C_f and St are equivalent to that for a flat- plate flow with constant pressure and constant wall temperature

-any chemical reactions in the B.L affect only the driving potential or enthalpy in this case

The boundary layer analysis is carried out with the classic parameters: Re, Pr, Nu, St and C_f. Von Karman's form of Reynolds' analogy is used as given in [11].

The possible sources of error from the listed assumptions are identified in the following discussion. The C_f and St number flat plate approximations with constant axial pressure gradients could cause some variations from the actual conditions as a nozzle is has axially varying pressure gradients and an inclined surface. The combustion process will most likely continue, resulting in a higher total temperature than was achieved in the combustion chamber.

B. Nozzle Wall Temperature

In this section, steady state wall thickness for heat fluxes near what has been shown in the section above and the corresponding estimated temperature profiles will be developed via a CFD study using COMSOL. This section is important as it will illustrate the expectation that the wall will initially reach temperatures above the expected ablation temperature at which point the walls will ablate down to a new steady state thickness. At this new steady state thickness the walls will be kept cool enough to eliminate nozzle ablation.

a. Setting up a Finite Element Analysis

The nozzle wall steady state temperature profile will be evaluated just prior to the throat as the maximum heat load will be imposed here. This was illustrated in Fig. 11 above. A finite element study to determine the temperature profile in the nozzle wall is set up below. COMSOL® was used to perform the study, and the geometry with the program generated mesh is displayed below in Fig. 12.

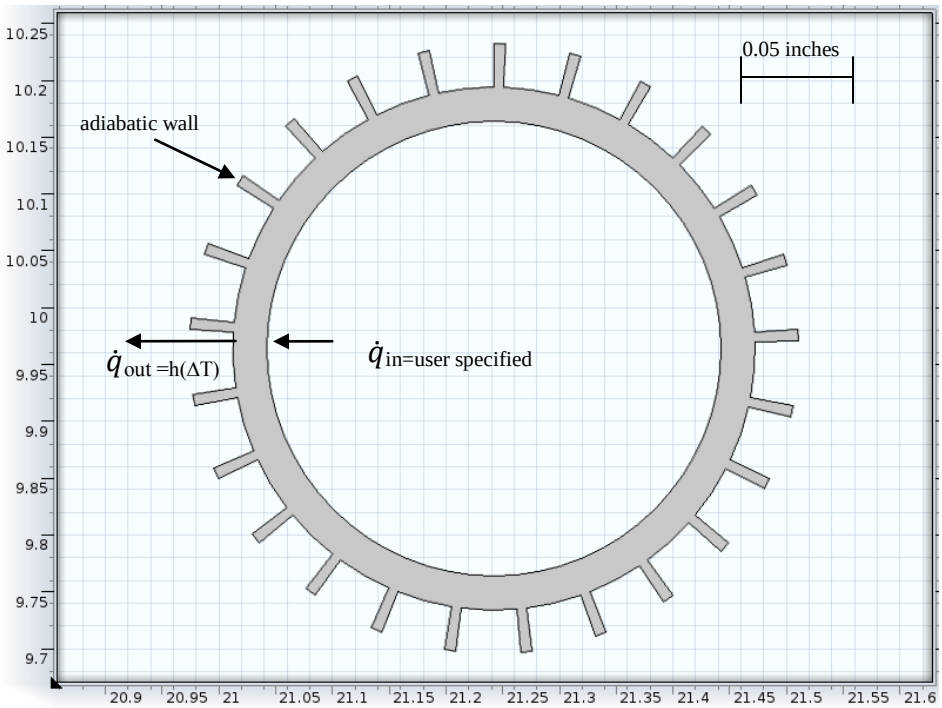

Figure 12 Nozzle cross section used for the COMSOL study.

Table 5: Inputs for the Finite Element Study on Wall Temperature

$\dot{q}_{max}$, btu/in^2-s	h_c , btu/in^2-s-R	k_{wall} , btu/in-s-R	$T_{wall\ intial}$, ^oR	$T_{coolant}$, ^oR	Wall thickness, in
6.25	0.0135	$=T*10^{-7}+6*10^{-5}$	529.67	529.67	0.040

Inputs to the study are specified above in table 5. The heat flux was chosen as the average between the two solutions presented previously in Fig. 11. The determination of the thermal conductivity as a function of wall temperature used in table 5 is shown below in Fig. 13. The coolant initial temperature was specified as room temperature. This in meant to simulate an un-cooled oxidizer feed system as well as an ambient initial wall temperature. The coolant heat transfer coefficient was taken from previous studies on nitrous oxide cooled rocket nozzles[21,22]. In order to confirm the applicability of the coolant side heat transfer coefficient from the experiment in [21] to this study, a Nusselt number analysis was carried out[22] using the Dittus-Boelter Nusselt number correlation for a heated liquid. This is shown below in Eq. 22 as well as Nu correlation to h in Eq. 23. D_h in Eq. 23 is the hydraulic diameter as the cooling channels are not perfectly circular. The results of this analysis are plotted versus coolant velocity in Fig. 14.

$$Nu = 0.023Re^{0.8}Pr^{0.4} \quad (22)$$

$$Nu = \frac{hD_h}{k} \tag{23}$$

The values for thermal conductivity were found in [23] plotted and fitted in Fig. 13 to generate the relationship versus temperature displayed in table 5.

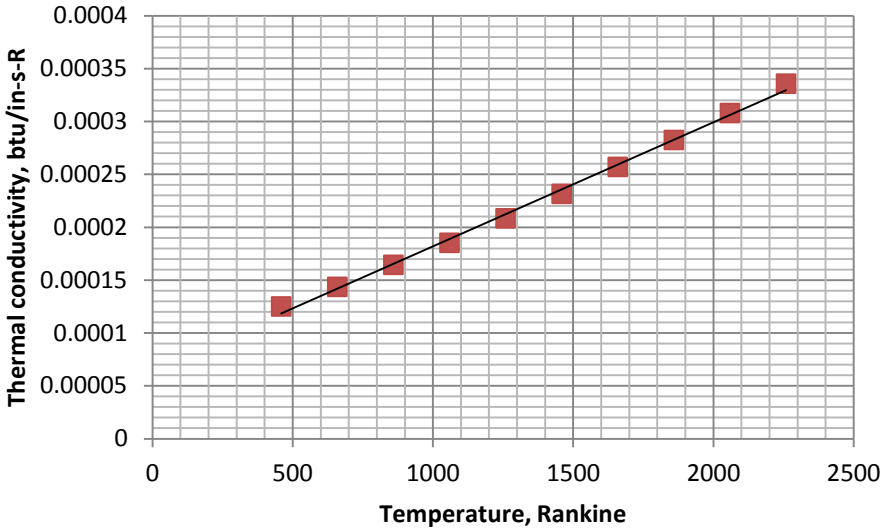

Figure 13. The curve fit of thermal conductivity for Inconel 625, k versus temperature R^2=0.997

The results of the heat transfer prediction using Eqs. (22) and (23) are shown and compared for nitrous oxide and water below.

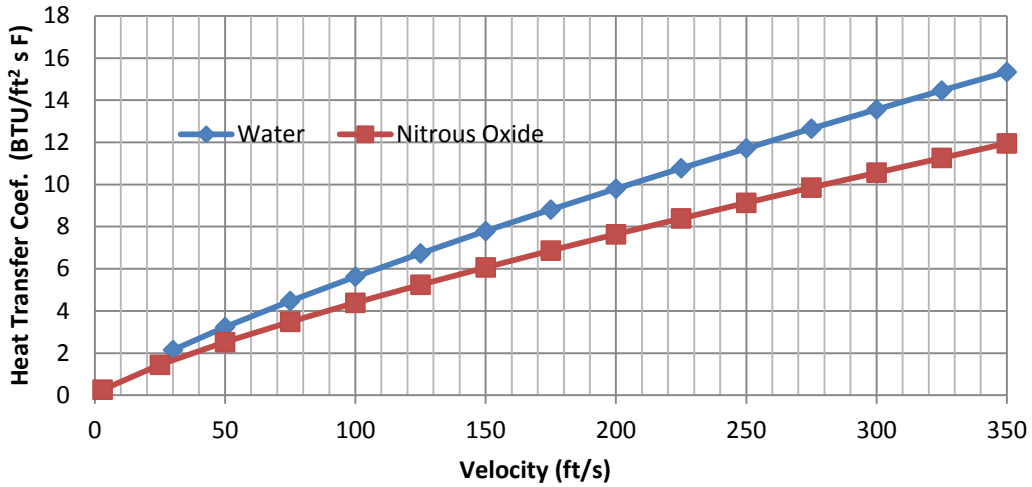

Figure 14 heat transfer coefficient for nitrous oxide and water as a function of flow velocity at a fixed pipe diameter (Re<10,000). Figure 14 taken from [16]

b. FEA Results

A solution using the specified inputs were then generated and is shown below in Fig. 15. This temperature profile shows temperatures well above the thermal limit of the material. However, below the surface, the inner wall is below that limit.

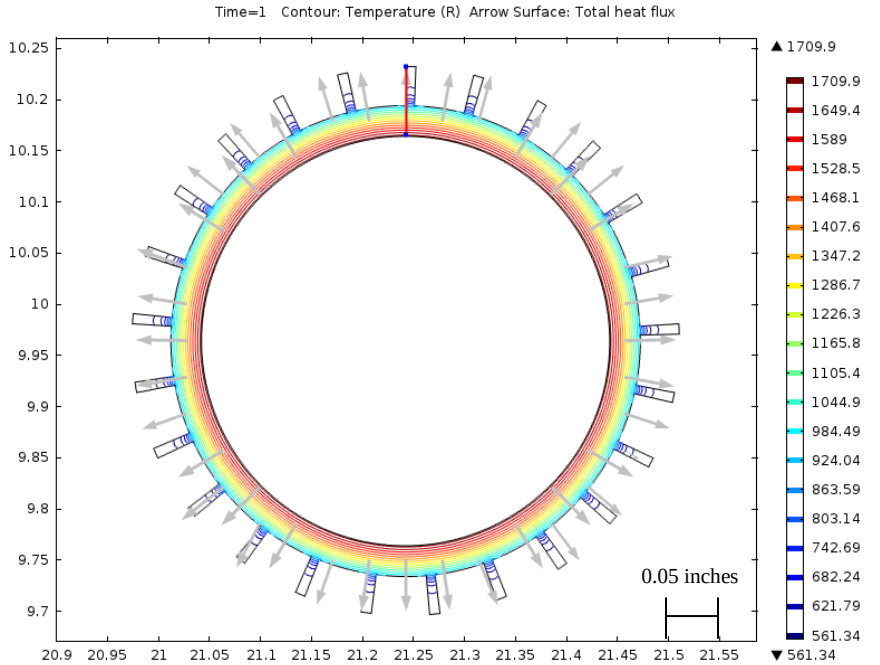

Figure 13. Wall temperature profile for the conditions specified in table 5. Units on axes is inches

In order to determine if there is a steady state operational thickness for a similar heat flux where the wall temperature was maintained below its thermal limit, a similar study with a thinner wall thickness of 0.011 in was conducted. The results are shown below in Fig. 16. By examining Fig.16 , you can see a steady state thickness has been reached. So long as the nozzle ablates smoothly, it can continue to operate relatively unaffected after it reaches that thickness.

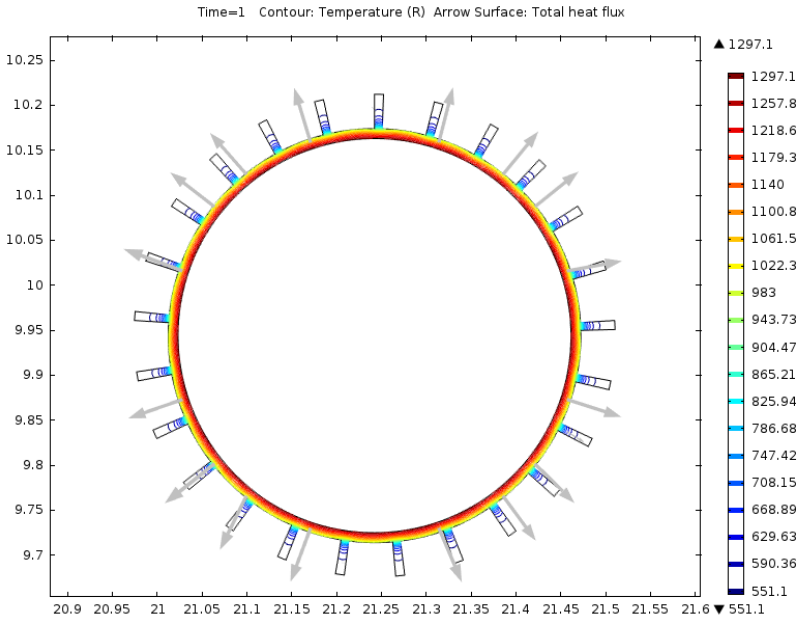

Figure 14 Temperature profile for an identical nozzle with w_t= 0.011 in

The results of the study on a wall ablated to 11 thousandths of an inch shows wall temperatures slightly below the thermal limit of 1559 R or 1100 F. The same wall thickness with an increased heat flux to 9 btu/in^2-s was then evaluated, and the results are displayed below in Fig. 17.

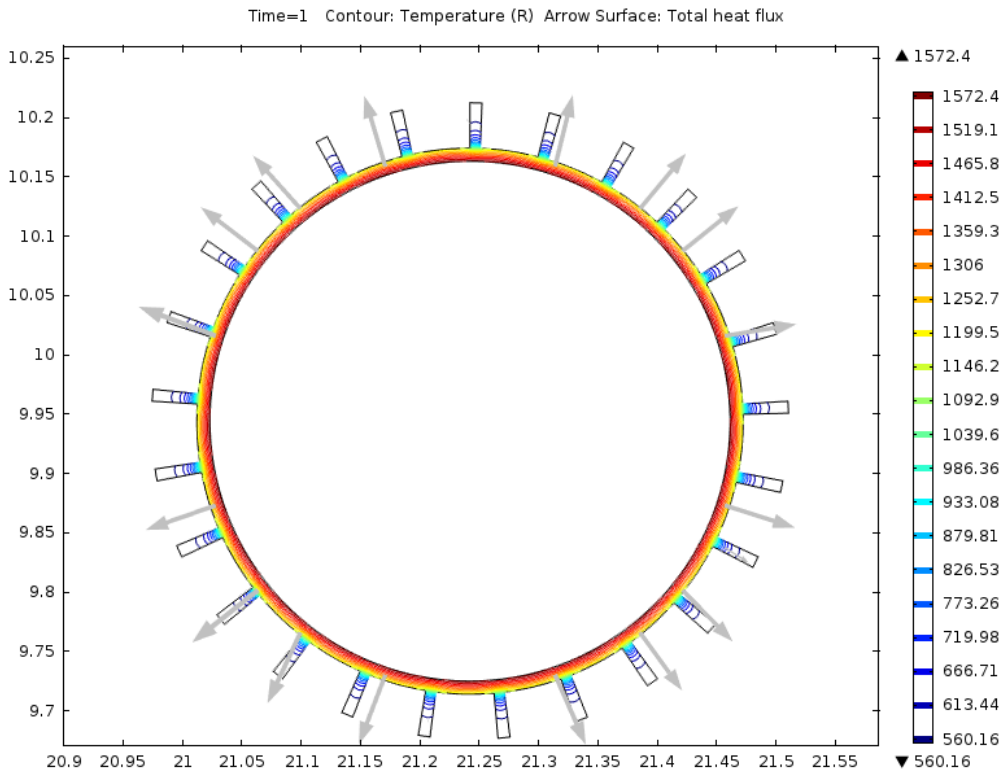

Figure 15 temperature profile for w_t= 0.011 inch and $\dot{q}$=9 btu/in^2-s
units on axes are inches

Two particular questions surface when examining the analytical results: 1) What is the wall's response to gradually increasing the heat flux up to and then beyond the materials' thermal limits? 2) What is the response if the nozzle were immediately subjected to heat loads beyond the 40 thousandths inch thickness limit? It is unknown whether the wall would regress in an orderly fashion, layer by layer or if the sub-layer would begin to melt and cause the walls to deform. If this were extreme enough the nozzle would be likely to lose effectiveness. For example, if the nozzle deforms, shocks or flow separation may form along the distorted walls causing a loss of thrust. These are very important drivers for conducting the experiment.

If the walls do regress in an orderly manner, it would appear as though a much higher operational heat load could be withstood by the cooled nozzle. If this is the case the ultimate withstand able heat load could be much higher than anticipated without degradation.

It can be seen by the comparison of Figs. 15-17 that if $\dot{q}$ is high enough, the wall will ablate until it reaches a steady state thickness which is a function of heat flux. As the flux increases, the wall thickness for steady state heat transfer decreases.

It is now useful to know the minimum wall thickness for operation. The value of maximum shear stress at an elevated temperature of 1200 F is 82 ksi[15] allowing for a minimum wall thickness at a 600 psi pressure difference of less than 600 millionths of an inch with a factor of safety of 2. This is shown at the end of Appendix C. With this in mind the structural limit will be set aside as it appears that a thermal failure is the most likely.

C. Experimental Setup

To validate our models of nozzle heating, an experiment was devised and executed. In a flight weight vehicle with the proposed aft-end vortex injected, regeneratively cooled nozzle, the design and integration can be quite complex. Added to this is the desire to eliminate any unnecessary weight. Neither is necessary for a productive experiment. With the experimental objectives in mind, modifications are made to the coolant, oxidizer and injection methods.

The primary experimental goals are to evaluate the response of a cooled rocket nozzle at, and even past, the nozzle's expected limits. Additional objectives are to validate the analytical models as a means to evaluate and modify future designs. The following sections lay out the adjustments made in the interest of simplifying and expediting the experimental procedure, easing the risk factors and pinpointing the desired results.

a. Experimental modifications

i. Injection Scheme

For financial and time considerations, traditional head-end injection was used, as the necessary components are already in place on the test stand. This was primarily done in an attempt to expedite the experimental setup, allowing more time for experiment and analysis. As there will be no aft-end injection, there was also no regenerative heating of the oxidizer before it was introduced to the combustion chamber. The cooling circuit will be independent of the rest of the rocket and is used exclusively to cool the nozzle and to measure the heating distribution.

ii. Oxidizer

Due to recent events with unintentional explosions at Nitrous Oxide testing facilities and the author's unfamiliarity with the oxidizer, air and gaseous oxygen was used as alternative oxidizers. Nitrous Oxide dissociates exothermically creating a potential hazard[28]. Gaseous O_2 has been used extensively, but the fairly low traditional regression rate characteristics of hybrids render low O/F ratios difficult. Oxidizer to fuel ratios above the stoichiometric ratios produce an oxidizer rich exhaust plume that can oxidize the nozzle wall and cause additional ablation contaminating the experimental results. For this reason, air was used primarily, as it has a higher stoichiometric ratio with ABS which is nearly 10.5 for air compared to 2.5 for oxygen. This minimizes the risk of oxidation on the interior surface of the nozzle due to excess oxygen in the exhaust gases. O_2 will only be used as a supplement to the air as needed to reach higher heat fluxes and to assist in the ignition process.

iii. Coolant

Nitrous Oxide was replaced with water as the coolant for similar reasons as mentioned before with the oxidizer substitutions. Water served the experiment well as a coolant due to its availability and cooling capabilities. A benefit to this substitution was the increased specific heat, allowing for a more uniform water temperature as it passes through the cooling channels accepting heat from the hot wall.

iv. Calorimeter Nozzle

The calorimeter nozzle shown below in figure 17 was printed out of Inconel 625 using SLM at NASA Marshall Space Flight Center in Huntsville, AL. The throat area was similar to what was used in the previous analysis of chapter 2, requiring only minimal changes to the model. The cooling channels in this nozzle are running circumferentially instead of axially. A drawing of the nozzle is shown in Fig. 18, along with the specs of the nozzle in Table 6.

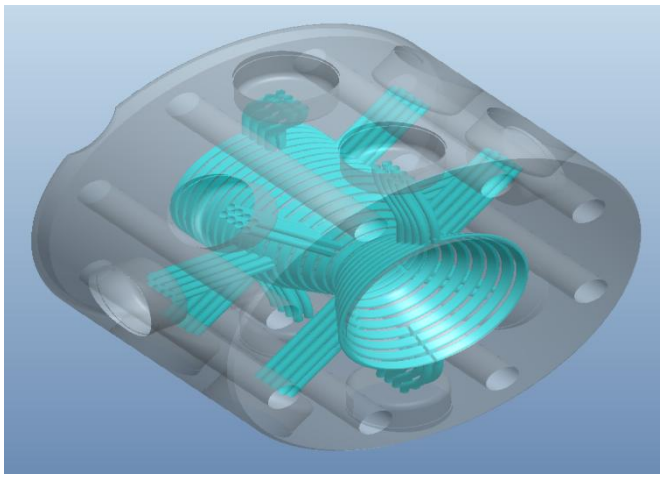

Figure 16 A semi-transparent model of the printed calorimeter nozzle to be tested

Table 6: Calorimeter Nozzle parameters

r^*, in	A_{exit}/A^*	r_{inlet}, in	wall thickness, in	Length, in
0.311	3.27	0.681	0.04	2.0

The circumferential cooling channels can be visualized by the light blue tubes in Fig. 17 and the parameters needed for the analytical model are given in table 6. This design will provide individual heat flux measurements at 6 independent axial sections. This proves useful, as the heat flux is expected to vary axially by more than 300% as shown previously in Fig 11. The

experimental heat flux calculation from the measured values of mass flow rate and water temperature is shown in Eq. 24.

$$\dot{q} = \dot{m} c_p [T_{water-out} - T_{water-in}] \qquad (24)$$

In order to obtain heat flux per unit area, the hot side nozzle surface area corresponding to each cooling station is shown in table 7 along with the coolant mass flow distribution. This is assuming that the nozzle wall has reached a steady state temperature profile where heat flux in is equal to heat flux out. Figure 19 illustrates the section of the nozzle cooled by each station.

Table 7: Inner wall cooling area per cooling inlet/outlet and coolant mass flow distribution

Station	1	2	3	4	5	6
Cooling Area, in^2	1.227	0.737	0.812	1.1549	1.215	1.215
% mass flow	15.80	17.95	17.79	16.57	15.88	16.01

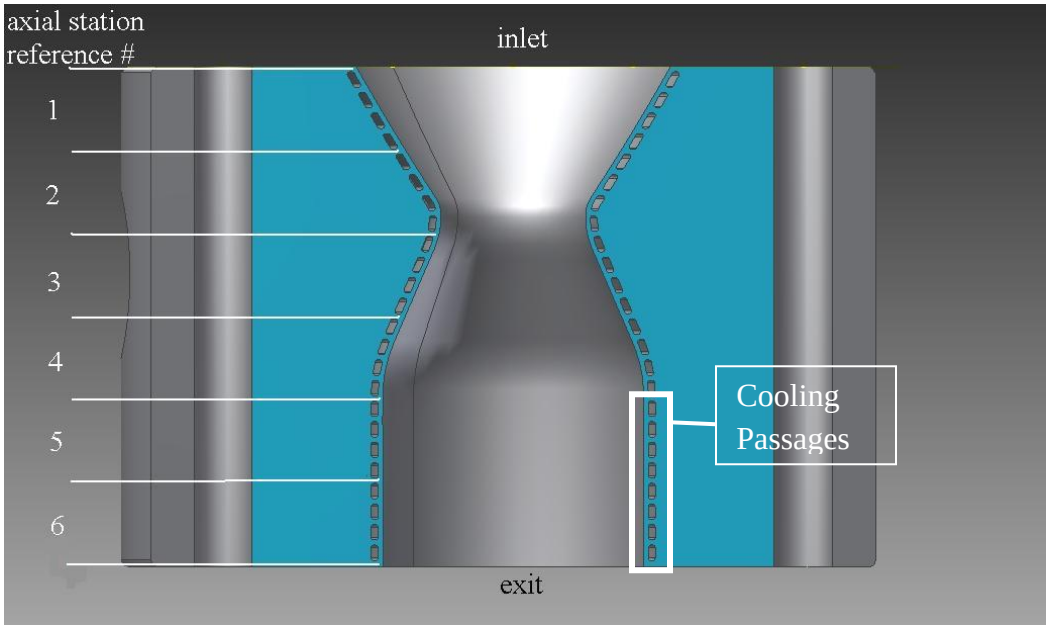

Figure 17 Cutaway view of the nozzle showing areas cooled by each station

The heat flux at each axial location as a function of temperature increase is shown below in Fig. 20.

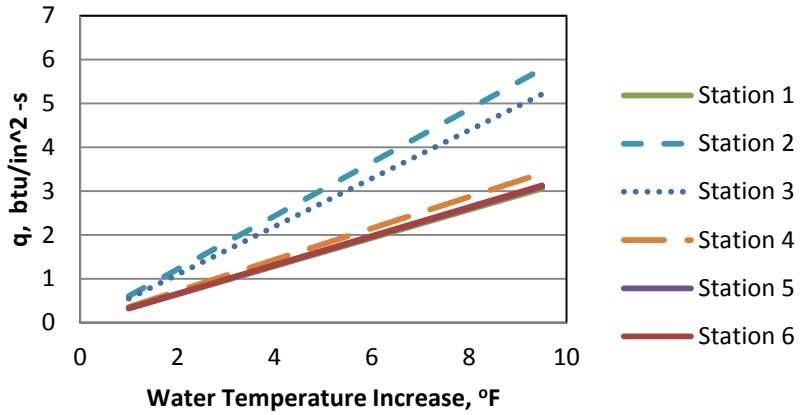

Figure 18 Heat fluxes associated with water temperature increase for each station

The coolant side heat transfer coefficient was approximated using the same Dittus-Boelter correlation used in generating figure 12. It is expected that the water was flowing 30-40 ft/s; corresponding to a heat transfer coefficient 30% higher than what was used in the nozzle wall temperature profile in COMSOL. A sample calculation corresponding to this is included at the end of Appendix C. A higher steady state heat flux may be realized as a result of the increased cooling.

b. Experimental Model

The analytical results for the rocket performance are illustrated on the following pages. These predictions not only provide a basis of what to expect with the modified configuration, but also will serve as a reference to validate or improve the analytical model.

Table 8: Adjusted Model Operational and Geometrical Specifications

r^* , in	$L_{fuel\ grain}$, in	$ID_{fuel\ grain}$, in	$OD_{fuel\ grain}$, in
0.311	12.0	0. 5	3.0

Table 9: Modeled Operational Conditions

$\dot{m}_{ox}$, lbm/s	P_c , psi	O/F	C_η	Thrust, lbs	C^* , ft/s	ISP , s
0.75	307.4	6.3-10.6	0.8	112.4	4209.5	133.7

Note: operational conditions are averaged over the steady burn time

In the figures below, the hitch that you see in the first couple of seconds is a result of the inaccuracies from the initial empirical regression rate correlation used to begin the run. The enthalpy balance regression rate is not used until the second time step. The time variation in the data is a direct result of the change in the O/F ratio. This is caused by the widening of the fuel grain port diameter during the run, which negatively affects the solid fuel regression rate. The O/F is also affected by the increase in burn area as the solid fuel grain regresses, but in this configuration, the effect of decreased regression rate overtakes that of the increased burn area.

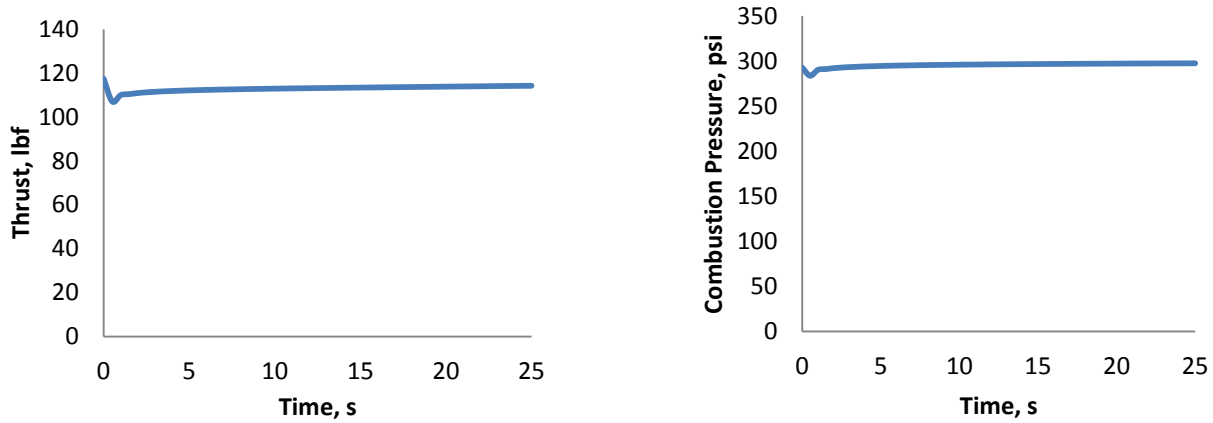

Figure 19 a,b Theoretical Thrust, Pressure curve for the thrust stand rocket as specified in tables 5 and 6.

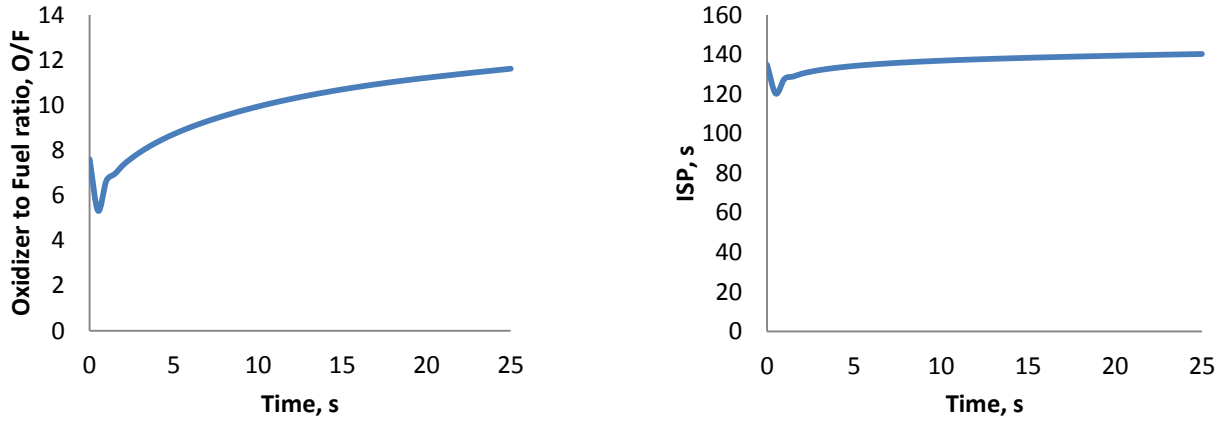

Figure 20 a,b O/F, ISP curve. Note: stoichiometric for Air and ABS ≈10.5

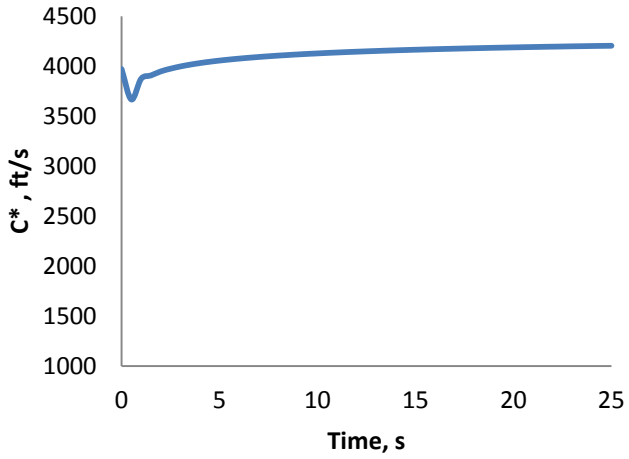

Figure 21 Analytical C* curves

The analytical heat fluxes from Bartz's relation are detailed in chapter 2 and shown for the described experimental model in Fig. 24 below. This is followed by the FEA study of the temperature profile in the 0.04 inch thick, cooled nozzle wall.

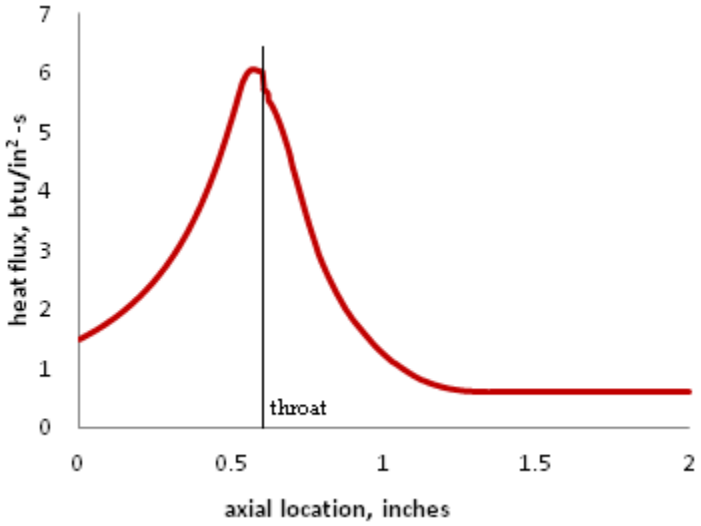

Figure 22. Heat fluxes from Bartz's relation. Throat @ 0.6075 in

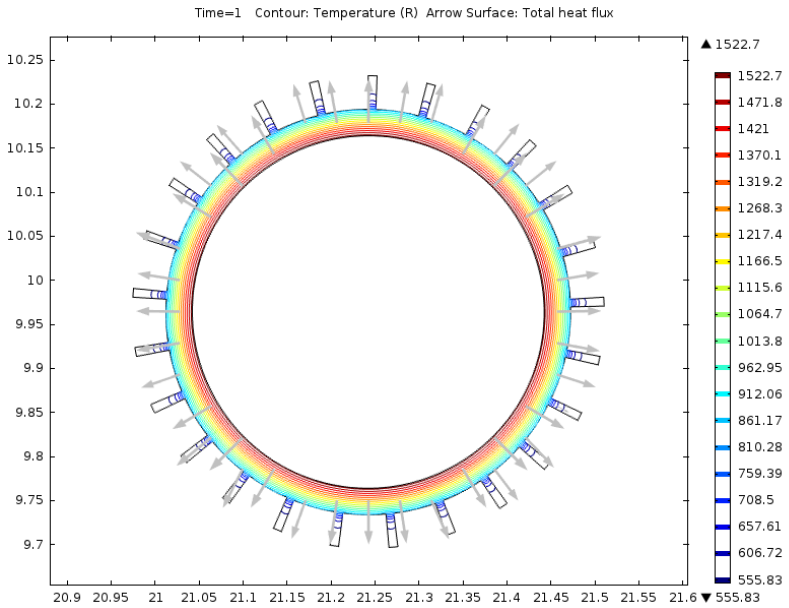

Figure 23. Temperature profile in the cooled nozzle wall with a specified heat flux of 5 btu/in^2-s

The results of the finite element study show the wall temperature near the previously designated thermal limit of 1559 Rankine. This shows that the proposed experimental configuration will generate thermal loads high enough to begin affecting the nozzle wall. This configuration is ideal for our experiment, as a slight decrease in mass flow rate will allow operation below the expected material limits. In addition, a slight increase to the oxidizer mass flow rate will push the thermal limits of the nozzle material and result in nozzle ablation.

Chapter IV
Experiment

This chapter lays out the physical setup and experimentation used in the experimental effort and then provides and analyzes the results. The experimental results presented in section C are from the initial tests and are intended to validate the model prior to pushing the limits of the calorimeter nozzle.

A. Setup/Procedure

A schematic of the physical setup and the wiring is displayed below. These can be seen in a larger format in Appendix B.

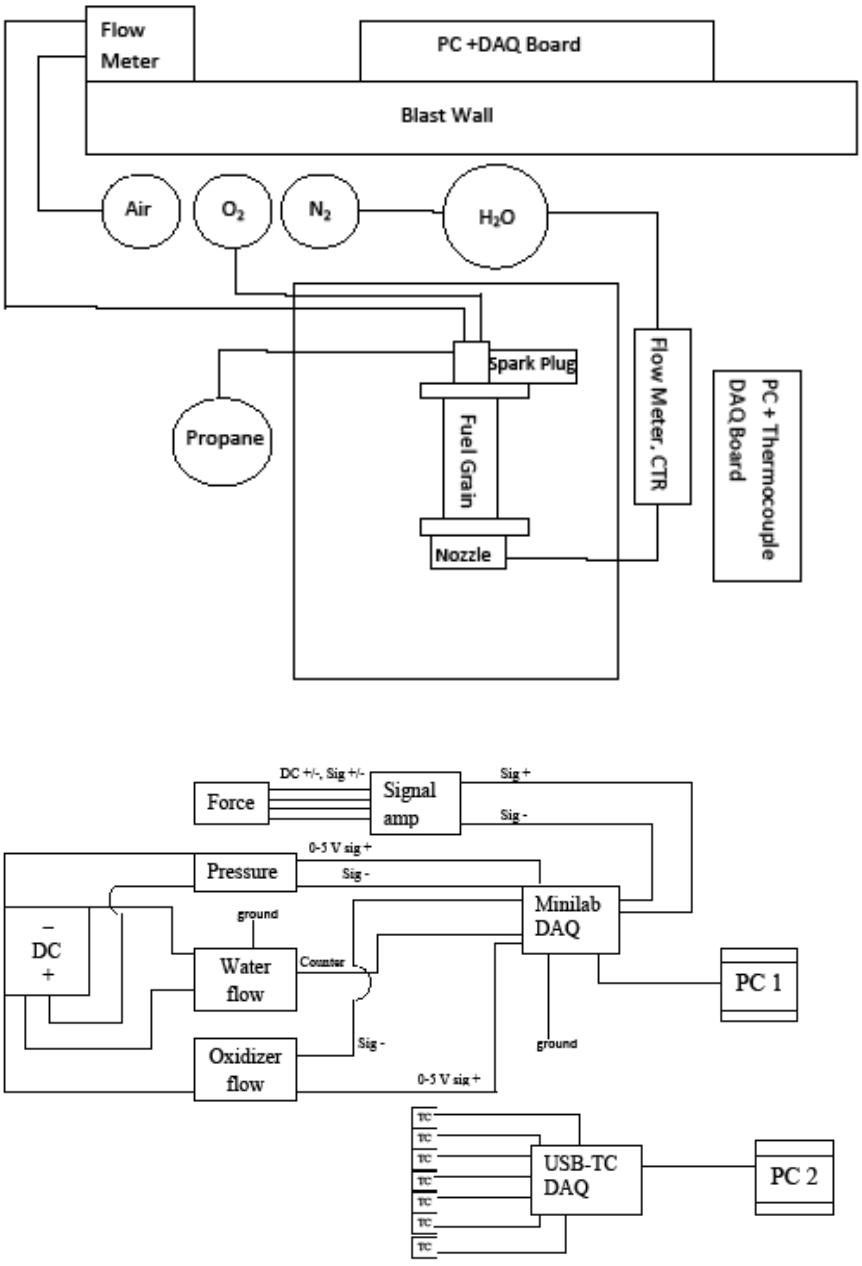

Figure 24 Schematic of the physical layout and wiring diagram

Figure 25 Assembled thrust stand

The propane tank on the ground paired with a spark plug and the green oxygen tank were used for ignition. The grey water tank was top pressurized at 500 psi with the black nitrogen tank. The yellow tank is the air, which serves as the primary oxidizer. The water jugs collect the water from each station, confirming measurements from the water flow meter and the percentage of water flow expected through each cooling circuit.

Figure 26 shows the backside of the blast wall.

The red box is the ball valve actuator used to control the air flow rate which is read from the display on the flow meter mounted on the backside of the blast wall. The flow meter is also linked to the data recording system allowing for the readings to be logged in real time.

Figs. 27 and 28 below, detail the calorimeter nozzle supply and measurement system. The single inlet thermocouple, shown in Fig. 28, serves as the reference temperature from which the six outlet thermocouples, shown in Fig. 27, are compared.

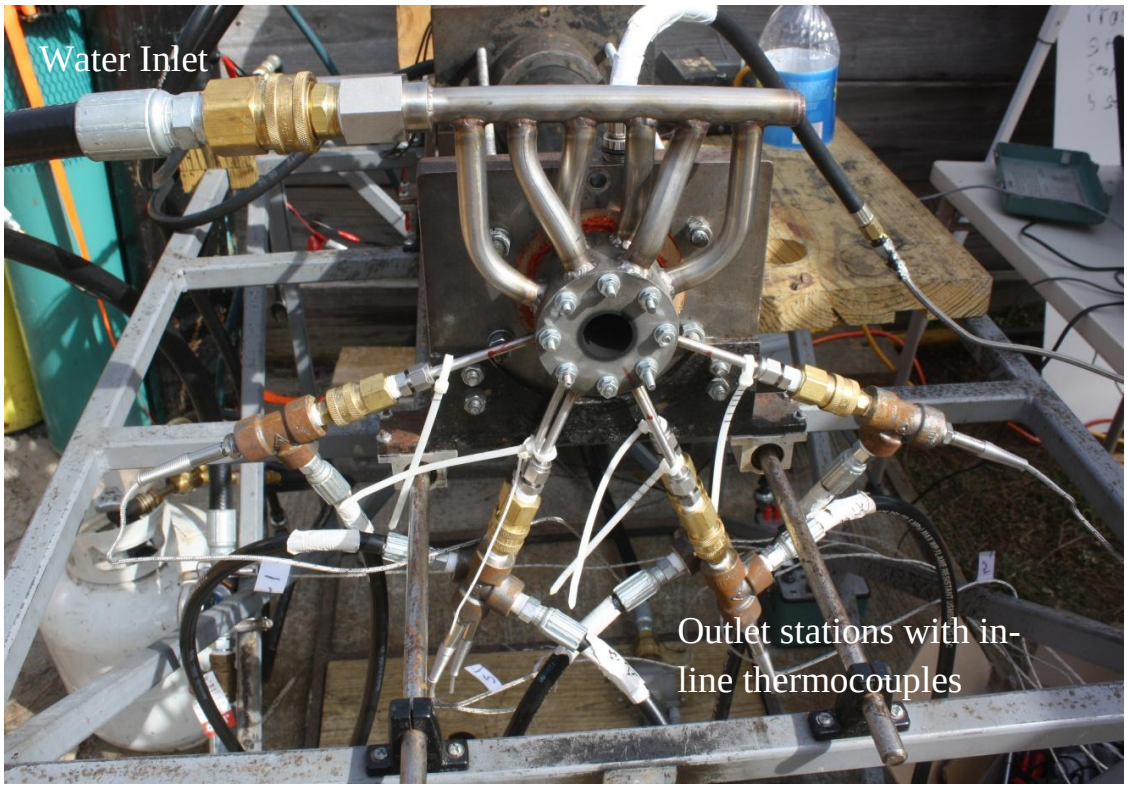

Figure 27 shows the calorimeter nozzle installed with the thermocouples for reading outlet temperature

Figure 28 reference/inlet thermocouple

B. Results/Analysis

To date, the experiment has been run 7 times with roughly 60 seconds of total firing time. Figure 29 below shows the experimental data from the second run and is supported with data from the analytical model in table 10.

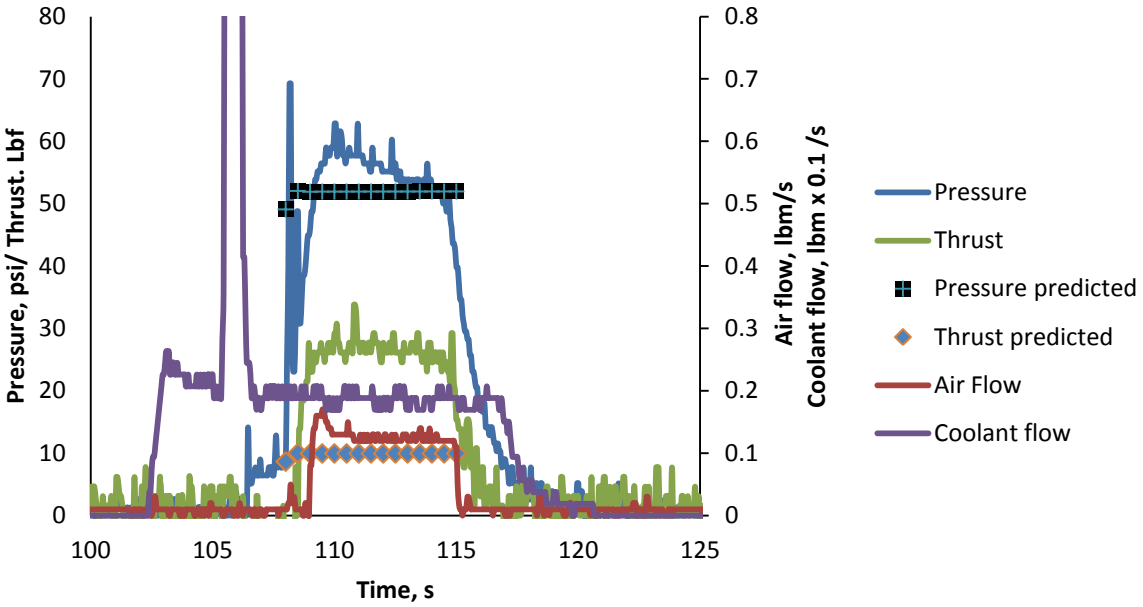

Figure 29 showing the experimental data from run 2.

The average experimental regression rate was 0.0064 in/s. The actual value was expected to be slightly lower than this as the ignition period was not accounted for. The results from the analytical model with identical oxidizer flow rates and initial/final grain diameters to the experimental run in Fig. 29 are shown below in Table 10.The initial and final grain radii are 1.075 and 1.115 inches, respectively. The time varying regression rates are illustrated allowing for a comparison of the predicted and experimental data.

Table 10 predicted conditions $\dot{m}_{air}$=0.125lbm/s, $r_{fg\_initial}$=1.075 in, r_{fg_final}=1.115 in

Time, s	Thrust, lbf	ISP, s	P_c , psi	O/F	$\dot{r}$, in/s
0	6.38	41.38	46.36	4.5884	0.010
0.5	7.52	54.06	49.17	8.8837	0.005
1	7.45	53.28	49.05	8.4037	0.005
1.5	7.46	53.42	49.07	8.4844	0.005
2	7.46	53.42	49.07	8.4849	0.005
2.5	7.47	53.43	49.07	8.4961	0.005
3	7.47	53.45	49.08	8.5054	0.005
3.5	7.47	53.47	49.08	8.5157	0.005
4	7.47	53.48	49.08	8.5254	0.005
4.5	7.47	53.50	49.08	8.5348	0.005
5	7.47	53.51	49.09	8.5446	0.005
5.5	7.47	53.53	49.09	8.5542	0.005
6	7.47	53.54	49.09	8.5634	0.005
6.5	7.48	53.56	49.09	8.5735	0.005
7	7.48	53.57	49.10	8.5826	0.005

The regression rate model used is deemed reasonable as the burn times are off by ¾ of a second for the specified range of grain radius at the head end. The data in Fig. 30 was a result of a 6.25 second burn where table 10 shows a 7 second burn time. This could be a result of the increased burn rate during the ignition process as 0_2 and propane were also injected into the combustion chamber to ignite the ABS. The thrust seen during the experiment is noticeably higher than expected. The higher than expected thrust measurements are believed to be a result of improper calibration procedures.

The results from run 1 are shown below in Fig. 30 along with the temperature and heat flux measurements in Figs. 31 and 32.

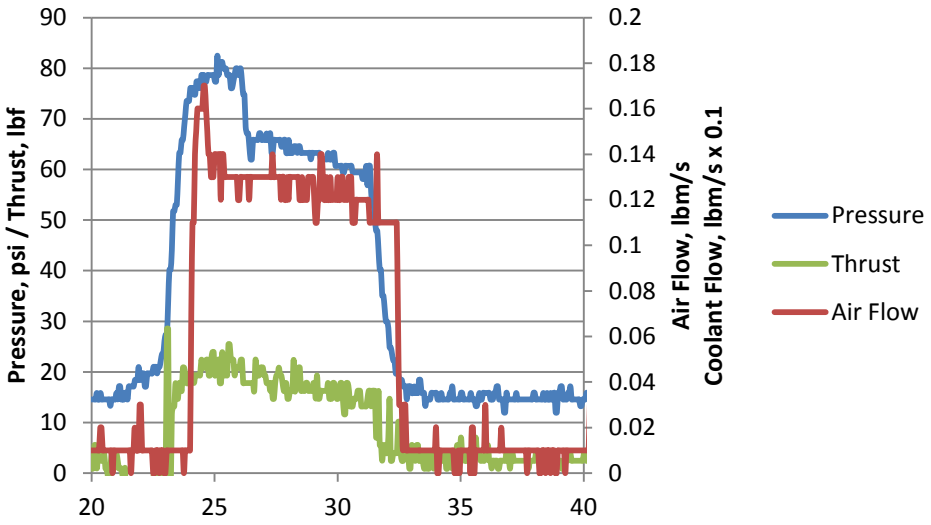

Figure 30 run 1 performance data

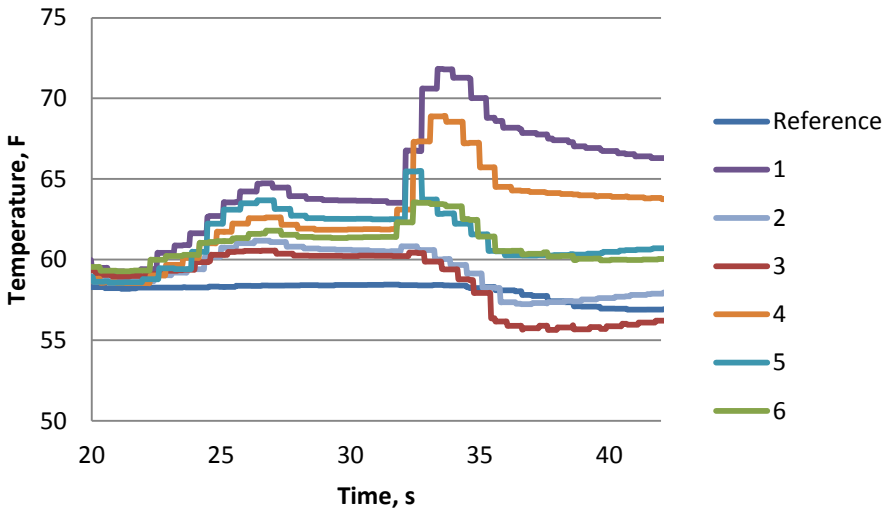

Figure 31 coolant temperatures at the inlet/outlets from run 1

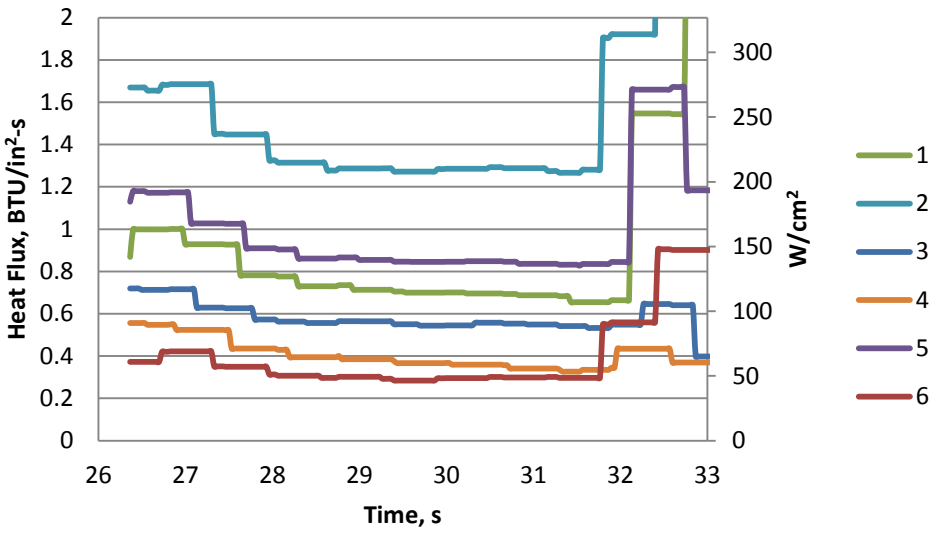

Figure 32 showing the heat flux at each axial station from run 1

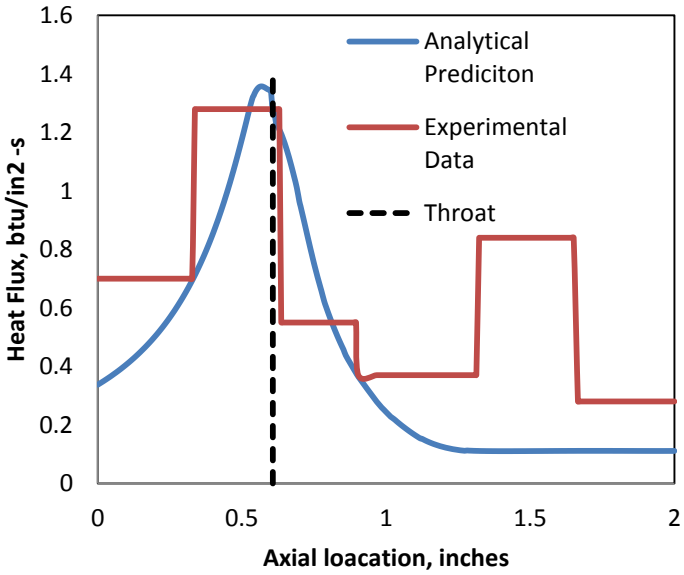

Figure 33 Predicted/experimental heat flux comparison via Bartz's method.

For comparison, the predicted heat fluxes at run 1 conditions are displayed above in Fig. 34. The predicted and experimental heat fluxes which are of primary interest, appear to compare very well with one another. This is with the exception of station 5, where it appears a shock has formed causing a higher rate of heat flux. This is due to the low combustion chamber pressure for these operating conditions.

The inner nozzle wall surface has shown no signs of ablation to this point as you can see below in Fig 35a-b. This is good news, as the cooled nozzle isn't expected to begin to wear until the heat loads approach 4.5 btu/in^2-s.

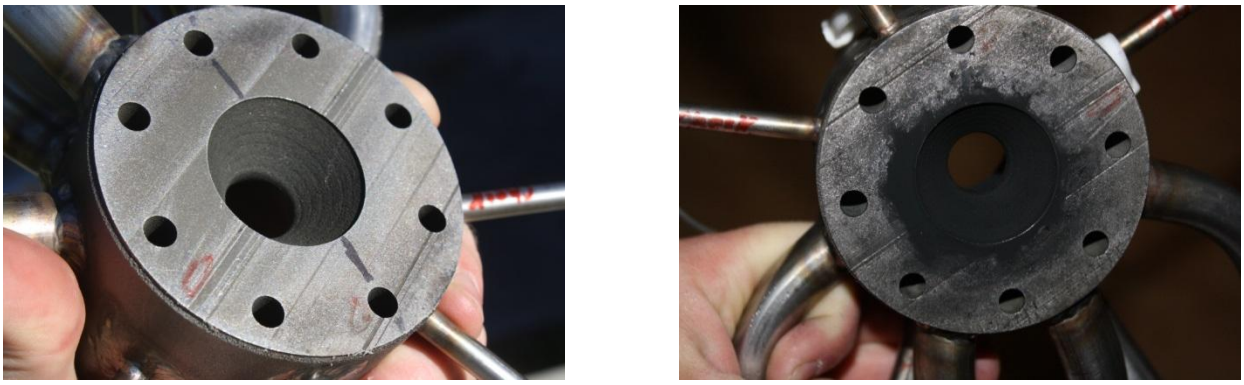

Figure 34 a,b The nozzle before and after.

Performance data and measured heat flux for runs 2 and 3 are displayed below in Figs. 35-36 a,b.

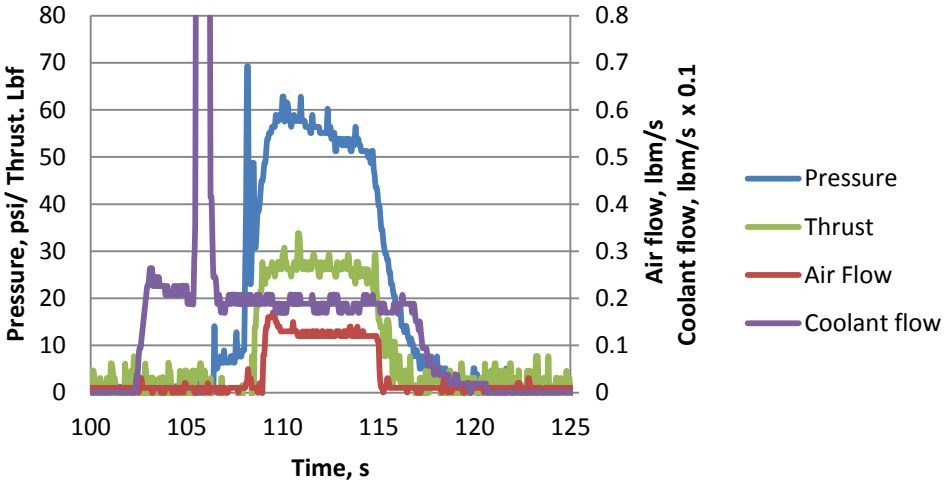

Figure 35a Performance data from run 2

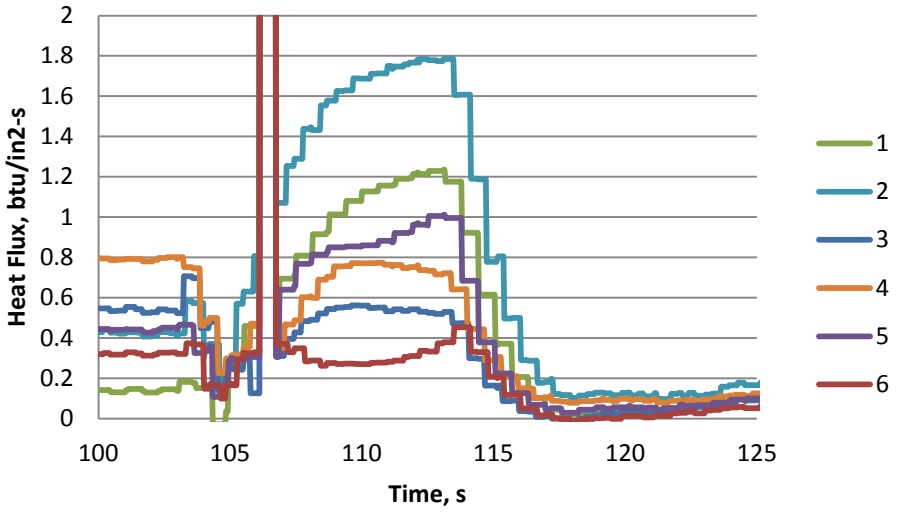

Figure 35b Heat flux during run 2

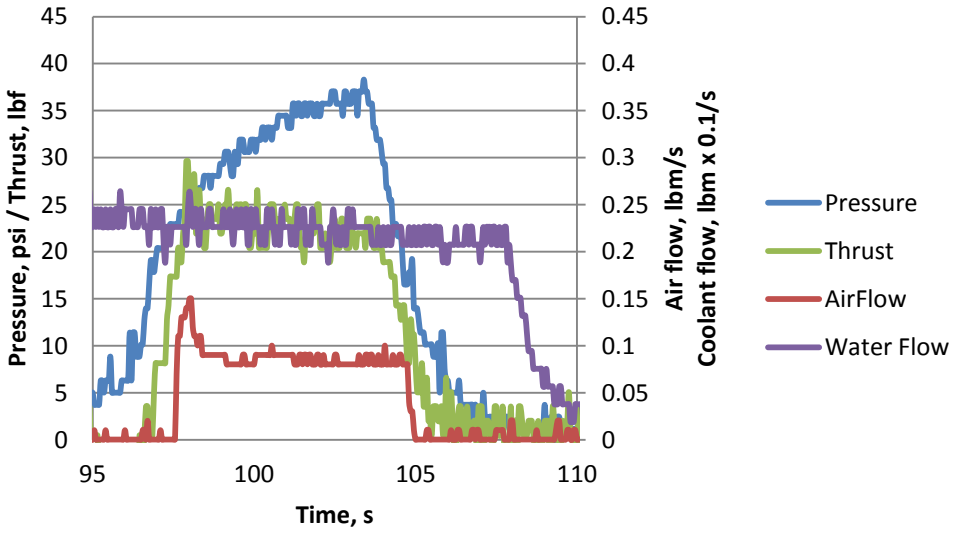

Figure 36a Performance data from run 3

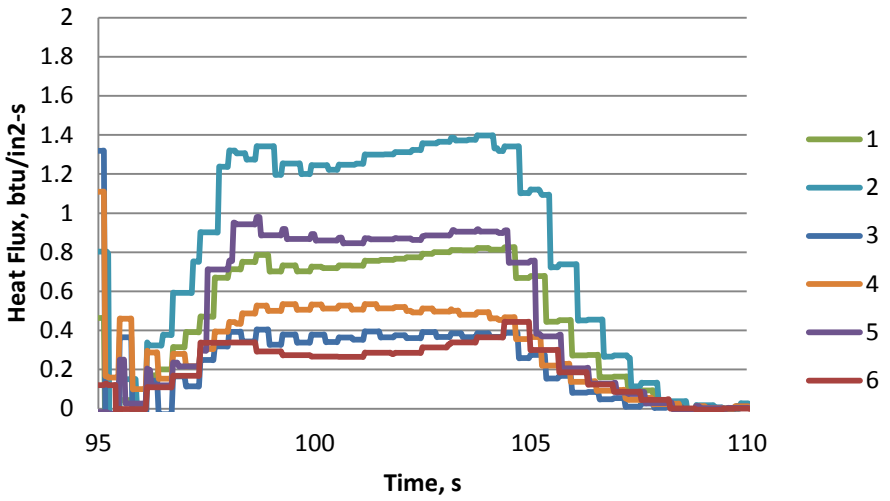

Figure 36b Heat fluxes from run 3

From the 3 runs shown, it can be seen that the experiment has been set up so that the results are reasonably repeatable.

D. Conclusions, Experimental and Design Methods Evaluation

The experiment has been set up and run, and the analytical model has been validated within reasonable accuracy. The modified head end, traditional regression rate model presented in chapter 2 has been validated for the geometry and conditions presented above. The experimental heat flux data agrees well with the predictions. Bartz's method has provided accurate predictions near the throat. The primary weakness of Bartz's method appears to be at the nozzle inlet. This limitation was expected[19], and due to the method's convenience and accuracy this will become the primary heat flux prediction method for the following experiments.

Chapter V
Final Remarks

A. Summary

Two hybrid rocket innovations have been examined and an investigation has begun with the objectives of improving performance and lowering costs for hybrid engines. Analytical tools for the design of a hybrid rocket and a cooled rocket nozzle have been developed, presented and evaluated. These are meant to serve as tools in follow-up work evaluating a regeneratively cooled rocket nozzle paired with an aft-end vortex injection scheme.

In the first of these investigations, an Aft-end vortex oxidizer injection has shown that a substantial increase in performance can be realized with only an additional complication of the injection scheme. This hurdle has been shortened by the improvement of rapid prototyping techniques that can repetitively reproduce complicated pieces, such as a regeneratively cooled nozzle with the vortex injectors printed into it. A means for a universal method for evaluating AEVI performance has been proposed and is intended to further streamline the design process.

A 3-D printed, cooled nozzle has been designed, integrated and successfully tested on a hybrid engine. This concept shows promise in developing a cheap reusable rocket nozzle that can be launched into orbit and used repeatedly for station-keeping maneuvers or multiple trajectory corrections without the added weight of ablative materials, thereby inceasing the thrust to weight ratio and making room for more payload at launch.

B. Future work

Work is currently underway continuing the cooled nozzle study. Now that the design methods have been confirmed and the thrust stand with all of its instruments is in working order, the experiment can continue with the expectation of producing useful data concerning the failure point and modes of the 3-D printed, cooled nozzle.

It is expected that the insights from the completion of this experimental work will be used in the design of a 3-D printed, cooled nozzle that will inject its coolant directly into the combustion chamber, allowing for the realization of an aft-end vortex hybrid rocket with a regeneratively cooled nozzle.

References

[1] Nanolaunch, LLC. A Whitepaper on Responsive and Affordable Nano-Satellite Launcher." Premier Space Systems, Inc. 30 Nov. 2010. Web.
[2] G.P. Sutton, O. Biblarz, "Rocket Propulsion Elements," Seventh Edition, John Wiley and Sons, New York, NY 2001
[3] London, John R. Lt Col, USAF. LEO on the Cheap, Methods for Achieving Drastic Reduction in Space Launch Costs, Air University Press, Maxwell Air Force Base, AL, 1994
[4] Arif Karabeyoglu, J. Stevens, D. Geyzel, B. Cantwell, "High Performance Hybrid Upper Stage Motor," Space Propulsion Group Inc., Sunnyvale, CA, AIAA Joint Propulsion Conference and Exhibit, August 2011, San Diego, CA
[5] G. Story, "Large Scale Hybrid Motor Testing," Marshal Space Flight Center, Hunstville, AL, 2006
[6] M. Chiaverini, D. Gramer, W. Knuth, "Hybrid Rocket Engine and Method of Propelling a Rocket," http://www.google.com/patents/US20040068976, April 15, 2004, Google Patents, US Patent App. 10/630,091
[7] Thicksten, Zachary, Macklin, Frank and Campbell, John, "Handling Considerations of Nitrous Oxide in Hybrid Rocket Motor Testing," AIAA Joint Propulsion Conference and Exhibit, AIAA, Hartfort, CT, 2008
[8] Kruth, J.P.,Mercelis,P.,Froyen,L., and Rombouts,Marleen, "Binding Mechanisms in Selective Laser Sintering and Selective Laser Melting". University of Leuven,Dept. of Mechanical Engineering, Division PMA and Dept. of Metallurgy and Materials Engineering. August 2004
[9] Y. Hirata, S. Aso, T. Hayashida, R. Nakawatase, "Improvement of Regression Rate and Combustion Efficiency of High Density Polyethylene Fuel and Paraffin Fuel of Hybrid Rockets with Multi-section Swirl Injection Method," Department of Aeronautics and Astronautics, Kyushu University, Fukuoka, Japan, AIAA Joint Propulsion Conference and Exhibit, San Diego, CA August 2011
[10] S.D. Eilers, S. A. Whitmore, "Correlation of Hybrid Rocket Propellant Regression Measurements with Enthalpy-Balance Model Predictions," Journal of Spacecraft and Rockets, Vol. 45, No. 5, pages 1010-1020, October, 2008
[11] Frank M. White, *Viscous Fluid Flow*, Third Edition, McGraw Hill, Boston, MA, 2006, pages 489-490
[12] Eric Doran, Jonny Dyer, Kevin Lohner, Zachary Dunn, Brian Cantwell, Greg Zilliac, "Nitrous Oxide Hybrid Rocket Motor Fuel Regression Rate Characterization," AIAA Joint Propulsion Conference, Cincinnati, OH, 2007
[13] S.A. Whitmore, Z.W. Peterson, S.D. Eilers, "Analytical and Experimental Comparisons of HTPB and ABS as Hybrid Rocket Fuels," Utah State University, Logan, UT, 2012
[14] N. Bellomo, F. Barato, M. Faenza, M. Lazzarin and A. Bettella, D. Pavarin, "Numerical and Experimental Investigation on Vortex Injection in Hybrid Rocket Motors," University of Padua, Padova, Italy. CISAS, AIAA Joint Propulsion Conference and Exhibit, August 2 011, San Diego, CA
[15] W. H. Knuth, M.J. Chiaverinin, D.J. Gramer, J.A. Sauer, "Solid-Fuel Regression Rate and Combustion Behavior of Vortex Hybrid Rocket Engines," AIAA 99-2318, ORBITEC™, Madison, WI, 1999
[16] W.H. Knuth, D.J.Gramer, M. J. Chiaverini, J.A. Sauer, "Development and Testing of a Vortex Driven, High-Regression Rate Hybrid Rocket Engine," AIAA-98-3507-393, ORBITEC™, Madison, WI, 1998

[17] W.H. Knuth, D.J.Gramer, M. J. Chiaverini, J.A. Sauer, "Experimental Investigation of a Vortex-Driven High Regression Rate Hybrid Rocket Engine," AIAA-98-3348-625, ORBITEC™, Madison, WI, 1998
[18] W.H. Knuth, M. J. Chiaverini, J.A. Sauer, D.J. Gramer, "Solid Fuel Regression Rate Behavior of Vortex Hybrid Rocket Engines", Orbital Technologies Corporation, Madison, WI, 2002
[19]D.R. Bartz, "Heat Transfer from Rapidly Accelerating Flows", *Advances in heat Tansfer,* Vol. 2, Academic Press, New York, 1965, pages 2-97
[20]D.R. Bartz, "An Approximate form of Compressible Turbulent Boundary Layer Development in Convergent-Divergent Nozzles," Trans. ASME 77 1955
[21]Patrick Lemieux, "Development of a Reusable Aerospike Nozzle for Hybrid Rocket Motors," AIAA 2009-3720, California Ploytechnic State University, San Luis Obispo, CA, 2009
[22] Rachel Preston, "Heat Transfer Analysis," The University of Tennessee-Knoxville, Knoxville, TN, 2013
[23]"Inconel 625 Technical Data," High Temp Metals, Inc., URL:http://www.hightempmetals.com/techdata/hitempInconel625data.php#5 [cited 1 March 2012].
[24]Jones, Joseph, "The Raven," Marshall Space Flight Center, July, 2012
[25]AIAA 2012-0436 "Combustion in Hybrid Propellant Rocket Engine for Aerospace Specialization in Mechanical Engineering Curriculum". Central Connecticut State University, 2012
[26]A.Bottom, H. DeMint, S. Dernovshek, H. Mrema, A. Travis, K. Winstead, "Design of a Modified Hybrid Rocket Engine", University of Tennessee-Knoxville, May 2012
[27]Bonnie Mcbride, Sanford Gordon, NASA-Glenn Chemical Equilibrium Program CEA, Nov. 5, 1999
[28]Z. Thickstein, F. Macklin, J. Campbell, "Handling Considerations of Nitrous Oxide in Hybrid Rocket Motor Testing," SpaceDev Inc., Poway, CA, 92064, USA

Appendices

Appendix A
Calibrations/Instruments

Table 11 Instruments

Instrument	Model	Range	Accuracy
Thermocouples	TC-J-NPT-G-72	32-1383 ^{o}F	see Table 11
Water Flow meter	FPR 200	0-51 GPM	+/- 2% Fullscale
Gas Flow meter	FLR 9760D	50-500 SLPM	+/- 2% Fullscale
Pressure Transducer	Viatran 218	0-250 psi	+/-0.4% FS
Force Transducer	Tovey "S" type load cell	0-250 lbf	+/- 0.03% FS
A/D Board	MiniLab 1008	0-10V	0.02% FS

The thermocouple calibration is presented below. The thermocouples to be associated with each outlet (TC-1:6) are calibrated against the reference or inlet thermocouple (TC-0) before being installed. The average offset is the result of 8500 samples taken at varying temperatures. The maximum percent error was found for a coolant flow rate of 2.5 lbm/s and a heat flux of 1.5 btu/in^2-s. As the heat flux increases, the percent error for each station will decrease. Listed next to the thermocouple number is the axial station assigned to that TC.

Table 12 Thermocouple Calibrations Referenced to TC-0, all values in deg F

TC- #	1(A-3)	2(A-6)	3(A-1)	4(A-5)	5(A-2)	6(A-4)
Average offset	-0.25	0.01	0.03	0.25	-0.19	0.39
80 % Range of uncertainty	0.06	0.11	0.1203	0.12	0.08	0.12
100% Range of Uncertainty	0.12	0.24	0.17	0.25	0.12	0.28
Max % Error (100% range)	8.0	16.0	11.3	16.7	8.0	18.7

The response time can also be seen below in figure 32.

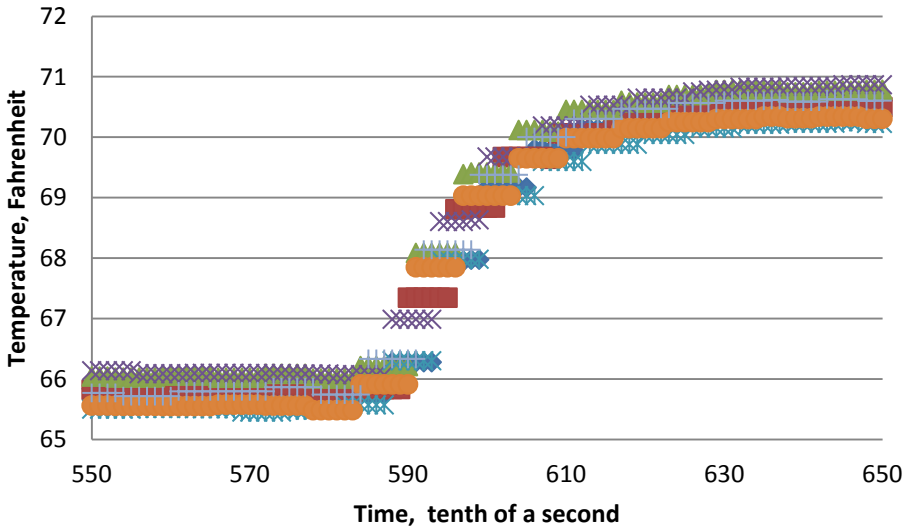

Figure 37 Response time visualization when exposed to a step temperature.

A response time of 5 seconds is displayed when transferred from one stagnate pool of water to another. This response time should decrease dramatically when exposed to forced convection due to the flowing water as opposed to natural convection in this case of still water.

The Pressure transducer calibration is shown below in table 13 and figure 38.

Table 13 Pressure Calibration

Volts	Pressure, psi
1.38	35
1.56	62
1.86	102
2.163	141.5
2.48	185
2.65	200

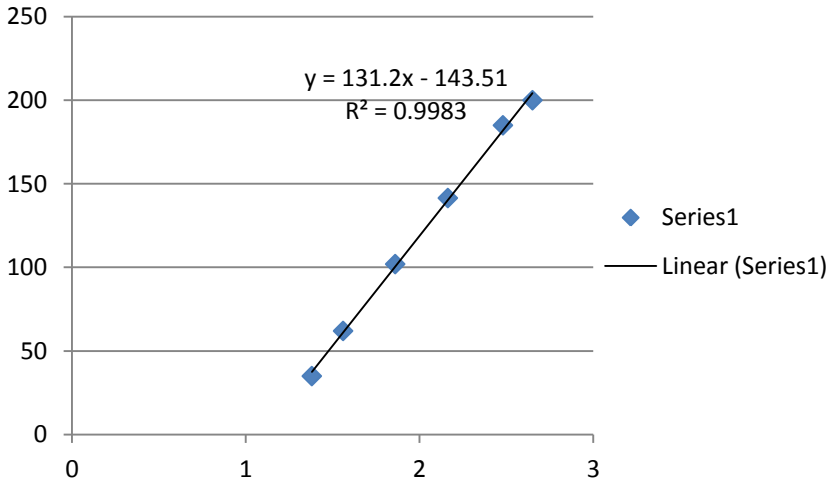

Figure 38 Pressure calibration plot

Appendix B
Thrust Stand Setup/Experimental Notes

Wiring Diagram

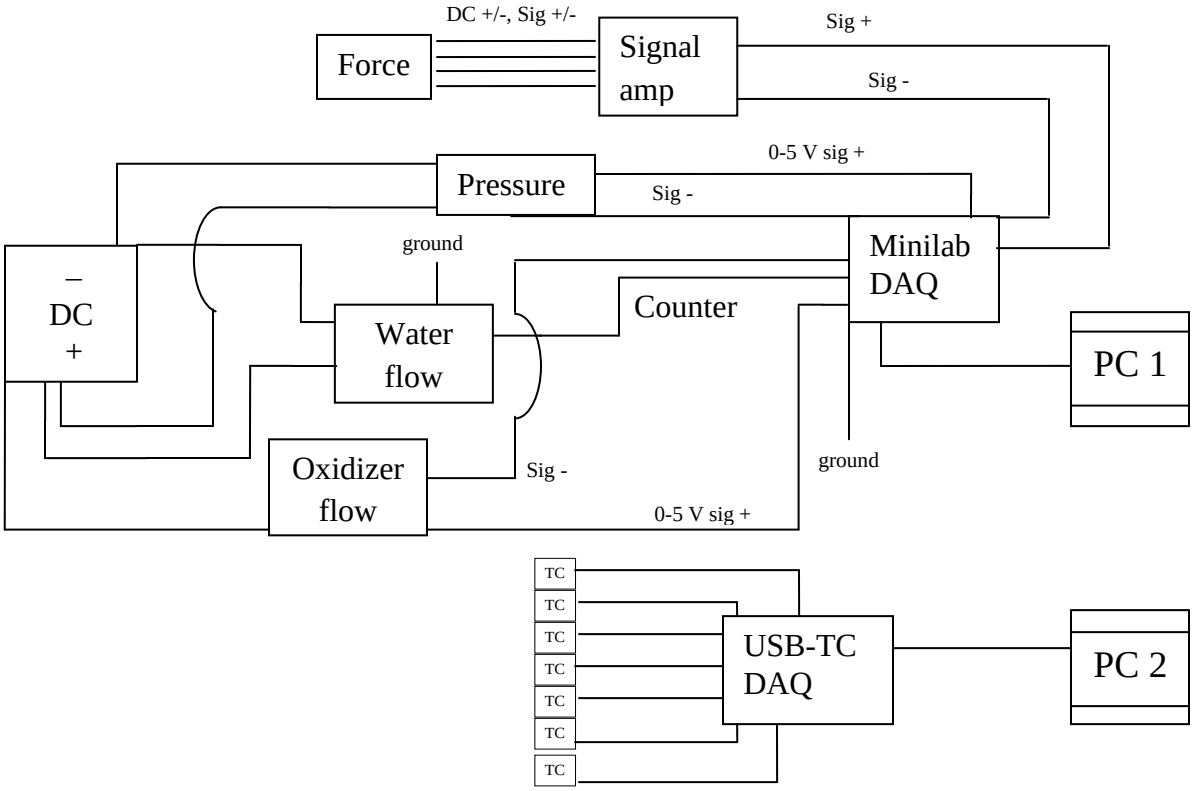

Figure 40 shows the wiring diagram above and the physical setup below

Physical setup

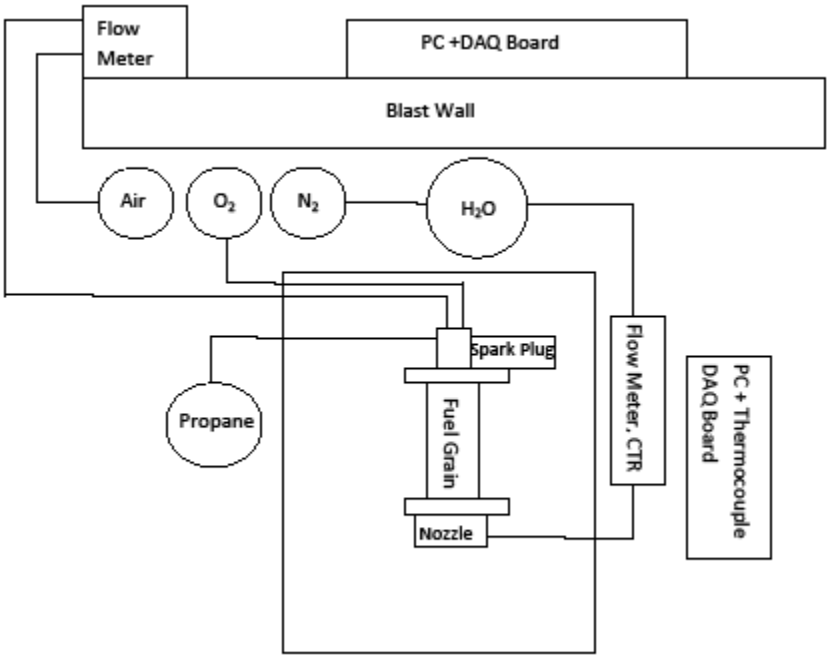

Figure 39 the wiring for the instruments and the physical setup above.

Experimental Notes

Electromagnetic Interference (EMI)

The spark plug and the fast acting solenoid valves (small black boxes with two wires), create a large amount of electromagnetic interference. When only running a few instruments, it does not appear to create too many problems. But with the complexity and number of recordings being made in this particular setup it was found that most instruments either needed to be shielded or grounded independently.

The counter (water flow meter) and the high pressure actuated ball valve were grounded to a lightning rod. This eliminated a majority of the problems as the stainless steel body of the counter absorbed a lot of this interference and was a large contributor to DAQ crashes. The DAQ board was also grounded in the same manner to an independent ground rod. This highly reduced the noise during experiment. The force transducer wire junctions were then shielded and the EMI was filtered via ferrite beads at the wire junction. The amplifier box was amplifying any EMI's so it was also critical that the force transducer wires were protected. This also greatly reduced the EMI that was initially causing the DAQ board to crash upon ignition. The image below shows the DAQ station shielded from the fast acting solenoid valves and the spark plug. You can see the Force transducer wire junction wrapped up with ferrite beads for EMI filtration and hanging on the wall before leading into the green amplifier box sitting next to the computer. The DAQ board is to the left of the computer and is grounded to the metal rod stuck in the ground.

Heat Flux Measurements

A few seconds of water run time prior to ignition is required for the thermocouples to reach a steady state temperature. By doing this to determine each TC's standard deviation from the reference temperature accurate heat flux data is more probable. Be sure the USB-TC reader is shielded from any sunlight or wind. Either of these can cause inaccurate and varying temperature measurements.

DAQ programs

TracerDAQ ran well and served all necessary purposes however, our version is limited to no more than 8 input channels. With 7 thermocouples and 4 other instruments this became a problem. Matlab can also be used for DAQ but will not accept counters or TC's if using measurement computing hardware. There is a patch allowing for the thermocouples to be used with MCC hardware but it was not implemented. The MATLAB DAQ code is provided in appendix C. Two computers also worked just fine and TracerDAQ is very common and easy to obtain. The Pressure, thrust, water flow and air flow data was collected at a sampling rate of 30 Hz while the temperature measurements were recorded at 2 Hz.

Appendix C
In-House Codes/ Hand Calculations

Hybrid Rocket Performance Code

Authors: Nick Quigley, Brian Hampton, Chris Potter Rocket Performance and Nozzle heat loads via D.R. Bartz closed form approximation

```
clc;clear all;
```

Initial conditions/Constants

```
tic
Oxidizer=5; %1=N2O 2=O2 3=75N225O2 4=air+o2 5=air
mdxy1=.125; %lbm/s

% Fuel Grain
hgrain=11; %Height of grain (inches)
rhoabs=0.0376; %density of fuel (abs)(lbm/in3)
Rout=1.115; %Outer grain radius (inches)
Rin=1.075; %Inner grain radius (inches)
min_wall_thickness=0.0; %inches
wall=Rout-min_wall_thickness; %stopping condition- ABS wall thickness
u=1; %regression rate manipulation


% Nozzle
rsi=.311; %inch radius
Aratio=3.27; %Nozzle area ratio =3 for sea level =20 for 70000 staying within
printing limits
Pa=14.2; %sea level pressure = 15 psi / @70000ft =0.6444 psi
eta=0.95; %nozzle efficiency
etastar=0.9; %combustion efficiency 0.8-0.95
Tflsrfc=523; %K melting temperature of ABS used value given in Whitmore's
JPP_june10_... paper
hvsldfl=2.3*10^6; %joules/kg latent heat of vaporization of Solid fuel
```

if you want to run different cases for different flow rates

```
for yu=1:1
    if yu==1
        mdotoxy=mdxy1;
    else if yu==2
            mdotoxy=mdxy2;
        else if yu==3
                mdotoxy=mdxy3;
            end
        end
    end
P0=60;%total pressure in psi inital guess
Pno=P0;
%if i==2.716
 %   Athroat1=.9298;
%else if i==3.56
```

```
 %       Athroat1=1.2061;
  %  else if i==4.47
   %         Athroat1=1.4764;
    %    end
    %end
%end

%Athroat1=1.13; %(inches^2)
%if mdotoxy==mdxy3
 %   Aratio=24
%else if mdotoxy==mdxy2
     %   Aratio=26
    %else if mdotoxy==mdxy1
   %     Aratio=38
  %      end
 %   end
%end
```

Empirical regression rate canstants (initial burn rate)

```
b=1;
j=1;


    a=u*0.06;
    n=0.54;


Moxy=0;
```

Calculations

check=1;

```
timestep=.5; %Defines time step (seconds)
count=0;
i=1;

fprintf('Time   Thrust Frozen    Thrust Equil     Thrust ave
ISP_frozen        ISP_equil      ISP_ave     OF_Ratio      mdot\n')
%initial values for regrate
%T0=3000; %K flame temperature using temperature in combustion chamber
adiabatic changes during run with O/F

%Cp=0.8569;%will be multiplied to go from cal/g to joules/kg
%mu=0.83293; %millipoise convert to lbm/in s in regrate eqtn
millipoise*0.672*10^-4/12=5.6*10^-6
%Pr=0.4838;
%dregs=1;
%mdotoxy_step=mdotoxy*timestep;
%ghy=1;
%Regrate=a*Gox^n; %Regression rate (inches/sec)
%Gox=(mdotoxy)/(hgrain*pi()*2*Rin);


while  Rin<wall; %lets the code run until of fuelgrain is at predetermined
minimun thickness
```

```
    mdotoxy_step=mdotoxy*timestep; %oxidizer mass flow for the timestep
(lbm/timestep)
    Gox(i)=(mdotoxy)/(pi()*Rin^2);%Uunits of mdot/Area (lbm/timestep/inch^2)
        reggin(i)=u*0.10404*(Gox(i))^0.681; %in/s
    if i==1
        Regrate=a*Gox(i)^n; %Regression rate (inches/sec)



    else if i>1

    %Regrate=u*0.047/(rhoabs*(Pr^0.1532))*(Cp*(4184)*(T0-
Tflsrfc)/hvsldfl)^0.23*(mdotoxy/(pi()*Rin^2))^(4/5)*((mu*5.6*10^-
6)/hgrain)^0.2;
    Regrate=(u*0.047/(rhoabs*(Pr^0.1532)))*(Cp*(4184)*(abs(T0-
Tflsrfc))/hvsldfl)^0.23*((mdotoxy)/((pi()*Rin^2)))^(4/5)*((mu*5.6*10^-
6)/hgrain)^0.2; %mu conversion: output in millipoise 1 millipoise=6.7197*10^-
5 lbm/ft-s  /12in/ft = 5.6*10^-6
    %Regrate=u*(1/2.54)*0.047/(rhoabs*27.68*(Pr^0.1532))*(Cp*(4184)*(abs(T0-
Tflsrfc))/hvsldfl)^0.23*((mdotoxy/.0022)/(pi()*(Rin*2.54)^2))^(4/5)*((mu*10^-
3)/(2.54*hgrain))^0.2;
    Lg=hgrain;
    Ac=pi()*Rin^2;
    Bez=13*(Pr^(2/3)-1);
    mdoto=mdotoxy;%+mdotoxy/(2*OFratio(i-1));
    trb=0.047*((mu*5.6*10^-6)*Ac/(mdoto*Lg))^(0.2)*(Cp*(4184)*(abs(T0-
Tflsrfc))/hvsldfl)^(-0.77);
    Regratefpo=u*(0.047*(mdoto/Ac)^(4/5)*((mu*5.6*10^-
6)/Lg)^(0.2)*(Cp*(4184)*(abs(T0-
Tflsrfc))/hvsldfl)^0.23)/(rhoabs*(1+Bez*sqrt(trb)));
    reg(i,1)=Regrate;
    reg(i,2)=Regratefpo;
    Regrate=Regratefpo;
        end
    end


    %Regrate=0.042/(Pr^0.1532*rhoabs)*(Cp(To-
Tflsrfc)/hvsldfl)^0.23*(cd*Ainj*sqrt(2rhoox*(Pinj-Po))/Achmbr)^(4/5);
    grainchange=Regrate*timestep; %how much grain changes during timestep
(inches)
    Rin_new=Rin+grainchange; %Inner radius after grain burn during timestep
(inches)
    mdotfuel_step=(Rin_new^2-Rin^2)*pi()*hgrain*rhoabs; %Fuel mass flow
    %rate (lbm/timestep)
    mdotfuel=mdotfuel_step/timestep; %total fuel mass flow rate

    OFratio(i)=mdotoxy_step/mdotfuel_step; %dimensionless
```

CEA

```
    %Input OF_ratio, P0 (P naught), and Ae/A* into CEA
    %Recieve output of gamma, C*, and a (sonic velocity)
    %Brian's CEA function
    %i=50;
    if Oxidizer==1
    CEAin(OFratio(i), Pno, Aratio);
```

```
%     CEAin(OFratio(i), P0, Aratio, 'ABS   C 3.85  H 4.85  N 0.43  wt%%=100.
h,j/mol= 62630.    t(k)=298.15', 'N2O wt%%=100. t(k)=298.15', 'psia',
'calories')
    [CstarT,CstarE,T0,Tt,Cp,GammaC,GammaT,GammaE, SonVelC,SonVelT,SonVelE,
rhoC,rhoT,rhoE, PC,PT,PE] = CEAoutd();
    else if Oxidizer==2
            CEAino(OFratio(i), Pno, Aratio);
    [CstarT,CstarE,T0,Tt,Cp,GammaC,GammaT,GammaE, SonVelC,SonVelT,SonVelE,
rhoC,rhoT,rhoE, PC,PT,PE] = CEAoutd();
        else if Oxidizer==3
                 CEAinn2o2(OFratio(i), Pno, Aratio);
    [CstarT,CstarE,T0,Tt,Cp,GammaC,GammaT,GammaE, SonVelC,SonVelT,SonVelE,
rhoC,rhoT,rhoE, PC,PT,PE] = CEAoutd();
            else if Oxidizer==4
                    CEAinairo(OFratio(i), Pno, Aratio);
    [CstarT,CstarE,T0,Tt,Cp,GammaC,GammaT,GammaE, SonVelC,SonVelT,SonVelE,
rhoC,rhoT,rhoE, PC,PT,PE] = CEAoutd();
                else if Oxidizer==5
                        CEAinair(OFratio(i), Pno, Aratio);
    [CstarT,CstarE,T0,Tt,Cp,GammaC,GammaT,GammaE, SonVelC,SonVelT,SonVelE,
rhoC,rhoT,rhoE, PC,PT,PE] = CEAoutd();
                    end
                end
            end
        end
    end
    %Cstar in (ft/s)
    %gamma dimensionless
    %SonVel in m/s
    %rho in grams/cm^3
    %Pressure in atmospheres
    SonVelC=SonVelC*3.28084; %Converting from meters/s to ft/s
    PE=PE*14.659; %converts PE from atmospheres to Psia
    PT=PT*14.659;
    PC=PC*14.659;
    oa=OFratio(i);
    fuelprcnt=(1/(1+oa))*100;
    T0=(etastar^(1/2))*T0;
    To(i)=T0;
    Tsh(i)=Tt;
    rhoc(i)=rhoC;
    gammac(i)=GammaC;
    asc(i)=SonVelC;
```

Throat Designation

```
%     Athroatnew=1/(P0*32.2/(.9*CstarE*(mdotoxy+mdotfuel)));
%     Athroat1(i)=Athroatnew;

    Athroat1(1)=rsi^2*pi(); %rthroat=0.
    rthroat=sqrt(Athroat1(1)/pi());
    Cstary(i)=(CstarE+CstarT)/2;
    Pnot(i)=etastar*Cstary(i)*(mdotoxy+mdotfuel)/(32.2*Athroat1(1));
    Pno=Pnot(i);
    oxprcnt=100-fuelprcnt;
```

for the next regrate calculation

```
    if Oxidizer==1
        CEAtpin(OFratio(i), Pnot(i), T0, fuelprcnt, oxprcnt);
    else if Oxidizer==2
            CEAtpino(OFratio(i), Pnot(i), T0, fuelprcnt, oxprcnt);
        else if Oxidizer==3
                oxoprcnt=.25*oxprcnt;
                oxnprcnt=0.75*oxprcnt;
                CEAtpinon(OFratio(i), Pnot(i), T0, fuelprcnt, oxoprcnt,
oxnprcnt);
            else if Oxidizer==4
                    oxoprcnt=0.08*oxprcnt;
                    oxnprcnt=0.92*oxprcnt;
                    CEAtpinairo(OFratio(i), Pnot(i), T0, fuelprcnt, oxoprcnt,
oxnprcnt);
                else if Oxidizer==5
                        CEAtpinair(OFratio(i), Pnot(i), T0, fuelprcnt,
oxprcnt);
                    end
                end
            end
        end
    end
    [mu, CP, Pr]=CEAtpout();
    Prandtl(i)=Pr;
    Cpj(i)=CP;
    Mu(i)=mu;

    %Regrate1=0.042/(Pr^0.1532*rhoabs)*(Cp(T0-
Tflsrfc)/hvsldfl)^0.23*(mdotoxy_step/(pi()*Rin^2))^(4/5)*(mu/hgrain)^0.2;

    %Prat=20/Pnot(i);
```

Performance Calculations

```
    time(i)=count;
    count=count+timestep;

    M=1; %Mach number=1 at throat of rocket
    gamma=(GammaT+GammaC)/2; %Average of the throat and exit gamma
    %Ma=sqrt((2/(gamma-1))*((1/Prat)^((gamma-1)/gamma)-1));
    %Aratio=(1/Ma)*((2/(gamma+1))*(1+((gamma-
1)/2)*Ma^2))^((gamma+1)/(2*(gamma-1)));
    %values for use in CT calculations
    CT_ideal_atm(i,j)=  sqrt(((2*gamma^2)/(gamma-1)) * ((2/(gamma+1))^...
        ((gamma+1)/(gamma-1))) *(1-(PE/Pnot(i))^((gamma-1)/gamma)))+...
        ((PE-Pa)/Pnot(i))*Aratio; %CT ideal equation on page 518 of
        %propulsion book.
    Thrust_equil(i)=eta*CT_ideal_atm(i)*Pnot(i)*Athroat1(1);%Calculates
thrust
    mdot(i)=mdotfuel+mdotoxy;
    Mf=aratiofunc(Aratio,GammaT); %Mach number for Aratio=28 (found from
secant method program aratiomunsta.m
    P0f=PT/0.5283; %Total Pressure
    PEf(i)=Pnot(i)/((1+((GammaT-1)/2)*Mf^2)^(GammaT/(GammaT-1))); %frozen
exit pressure
    CT_ideal_frozen(i)=  sqrt(((2*gamma^2)/(gamma-1)) * ((2/(gamma+1))^...
        ((gamma+1)/(gamma-1))) *(1-(PEf(i)/Pnot(i))^((gamma-1)/gamma)))+...
```

```
        ((PEf(i)-Pa)/Pnot(i))*Aratio;
    Thrust_frozen(i)=eta*CT_ideal_frozen(i)*Pnot(i)*Athroat1(1);%Calculates
thrust for frozen conditions
    CT_actual_atm(i)=Thrust_frozen(i)/(Pnot(i)*Athroat1(1));%Actual CT value
    ISP_equil(i)=Thrust_equil(i)/(mdot(i)); %ISP Equilibrium
    ISP_frozen(i)=Thrust_frozen(i)/mdot(i); %Frozen ISP
    Thrust_ave(i)=(Thrust_frozen(i)+Thrust_equil(i))/2; %Average of thrusts
    ISP_ave(i)=(ISP_equil(i)+ISP_frozen(i))/2; %Average of ISP's
    Rolder=Rin;
    Rin=Rin_new;
    gammastore(i)=gamma;
    fprintf('%3.2f   %6.4f     %6.4f       %6.4f     %6.4f      %6.4f
%6.4f    %6.4f   %6.4f   %6.4f  %6.4f %6.4f %6.4f\n',...
        time(i), Thrust_frozen(i), Thrust_equil(i),...
         Thrust_ave(i), ISP_frozen(i), ISP_equil(i),...
        ISP_ave(i), OFratio(i), mdot(i), Pnot(i), Gox(i), Regrate, Rolder)
    i=i+1;
    Moxy=Moxy+mdotoxy;
0.00   8.5721     8.7145       8.6433     56.3055      57.2405     56.7730
4.5884   0.1522   49.0827  0.0344 0.0097 1.0750
0.50   10.0138     10.0201       10.0170     71.9400      71.9854     71.9627
8.8050   0.1392   52.0391  0.0341 0.0051 1.0799
1.00   9.9398     9.9402       9.9400     70.9726      70.9753     70.9740
8.3049   0.1401   51.9079  0.0340 0.0053 1.0824
1.50   9.9533     9.9538       9.9535     71.1461      71.1498     71.1479
8.3899   0.1399   51.9324  0.0338 0.0053 1.0851
2.00   9.9529     9.9534       9.9532     71.1430      71.1465     71.1448
8.3890   0.1399   51.9317  0.0336 0.0053 1.0877
2.50   9.9552     9.9557       9.9554     71.1694      71.1730     71.1712
8.4005   0.1399   51.9357  0.0335 0.0052 1.0903
3.00   9.9560     9.9565       9.9562     71.1836      71.1872     71.1854
8.4100   0.1399   51.9372  0.0333 0.0052 1.0930
3.50   9.9579     9.9584       9.9581     71.2064      71.2100     71.2082
8.4202   0.1398   51.9408  0.0331 0.0052 1.0956
4.00   9.9595     9.9600       9.9597     71.2261      71.2298     71.2279
8.4296   0.1398   51.9437  0.0330 0.0052 1.0982
4.50   9.9609     9.9614       9.9612     71.2453      71.2490     71.2472
8.4393   0.1398   51.9463  0.0328 0.0052 1.1008
5.00   9.9620     9.9625       9.9622     71.2610      71.2647     71.2628
8.4486   0.1398   51.9480  0.0327 0.0052 1.1034
5.50   9.9634     9.9640       9.9637     71.2803      71.2841     71.2822
8.4584   0.1398   51.9506  0.0325 0.0051 1.1059
6.00   9.9649     9.9654       9.9651     71.2995      71.3032     71.3013
8.4682   0.1398   51.9532  0.0324 0.0051 1.1085
6.50   9.9666     9.9671       9.9668     71.3195      71.3233     71.3214
8.4774   0.1397   51.9563  0.0322 0.0051 1.1111
7.00   9.9675     9.9681       9.9678     71.3350      71.3388     71.3369
8.4869   0.1397   51.9578  0.0321 0.0051 1.1136
end
taverage=sum(Thrust_ave)/length(Thrust_ave);
mdtave=sum(mdot)/length(mdot);
ispavg=sum(ISP_ave)/length(ISP_ave);
ofratavg=sum(OFratio)/length(OFratio);

%pdfrnce=abs(Pnot(i)-P0);
%if pdfrnce>50
 %   display('did you account for the change in mdotox?')
```

```
%else
%end

Burntime=time(i-1);

b=1;
Time   Thrust Frozen    Thrust Equil     Thrust ave        ISP_frozen
ISP_equil      ISP_ave     OF_Ratio      mdot
end
```

Averaged results

```
eo=11;
b=length(time-1);
for eo=11:length(time)
    thrusty(eo-10)=Thrust_equil(eo);
    ispy(eo-10)=ISP_ave(eo);
    Cstaryy(eo-10)=Cstary(eo);
    Pnoty(eo-10)=Pnot(eo);
    OFy(eo-10)=OFratio(eo);

End
```

Nozzle Heat Flux calculations

```
nozzle_profile=dlmread('xy_jmax.dat'); %from file converter in matlab
directory
for i=1:117
nozzle_profile1(i,1)=nozzle_profile(i,1);
nozzle_profile1(i,2)=nozzle_profile(i,2);
end
nozzle_profile1(118,1)=(nozzle_profile(118,1)-
nozzle_profile(117,1))/2+nozzle_profile(118,1);
nozzle_profile1(118,2)=(nozzle_profile(118,2)-
nozzle_profile(117,2))/2+nozzle_profile(117,2);
for i=118:length(nozzle_profile)
    nozzle_profile1(i+1,1)=nozzle_profile(i,1);
    nozzle_profile1(i+1,2)=nozzle_profile(i,2);
end
rsi=nozzle_profile1(118,2);
T0=mean(To); %kelvin
Tthr=mean(Tsh);
Pr=mean(Prandtl);
Twh=1459; %rankine
Cstara=mean(Cstary);
gammas=mean(gammastore);
Pnots=mean(Pnoty);
OFratioave=mean(OFratio);
oa=OFratioave;
fuelprcnt=(1/(1+oa))*100;
oxprcnt=100-fuelprcnt;

if Oxidizer==1
        CEAtpinh(OFratioave, Pnots, T0, fuelprcnt, oxprcnt);
    else if Oxidizer==2
            CEAtpinoh(OFratioave, Pnots, T0, fuelprcnt, oxprcnt);
        else if Oxidizer==3
```

```
                oxoprcnt=.25*oxprcnt;
                oxnprcnt=0.75*oxprcnt;
                CEAtpinonh(OFratioave, Pnots, T0, fuelprcnt, oxoprcnt,
oxnprcnt);
            else if Oxidizer==4
                    oxoprcnt=0.05*oxprcnt;
                    oxnprcnt=0.95*oxprcnt;
                    CEAtpinairoh(OFratioave, Pnots, T0, fuelprcnt, oxoprcnt,
oxnprcnt);
                else if Oxidizer==5
                        CEAtpinairh(OFratioave, Pnots, T0, fuelprcnt,
oxprcnt);
                    end
                end
            end
        end
end
[mu, CP, Pr]=CEAtpout();
 % mu millipoise
 %cp cal/g-k
radc=0.1;
xthroat=0.6075;
omega=0.68; %0.6 for diatomic gases raised to 0.68 to account for monotomic
gases
[h, q, rloc, xloc, M, Thg]= nozzleheatflux(rsi, T0, mu, CP, Pr, Pnots,
Cstara, Twh, gammas, omega, radc, nozzle_profile1);
rloc=rloc*12;
xloc=xloc*12;

avgthrust=mean(thrusty);
avgisp=mean(ispy);
avgcstar=mean(Cstaryy);
avgpo=mean(Pnoty);
maxof=max(OFy);
minof=min(OFy);
Averages=[avgthrust avgisp avgcstar avgpo]
ofrange=[maxof minof]

figure(1)
plot (time,Thrust_equil,'b')

hold on
title('Thrust')
legend('Traditional','AEVI');
xlabel('time, s');
ylabel('Thrust, lbs');
b=b+2;
j=j+1;

figure(2)
plot(time,ISP_ave,'b');
hold on
title('ISP');
legend('Traditional','AEVI');
xlabel('time, s ');
ylabel('ISP, s');
figure(3)
```

```
plot(time,Pnot,'b')
hold on
title('Combustion Pressure');
legend('Traditional','AEVI');
xlabel('time, s');
ylabel('Pressure, psi');
figure(4)
plot(time,OFratio,'b')
hold on
title('O/F ratio');
legend('Traditional','AEVI');
xlabel('time, s)');
ylabel('O/F ratio');
figure(5)
plot(time,Cstary,'b');
hold on
title('Cstar')
legend('Traditional','AEVI');
xlabel('time, s');
ylabel('Cstar, ft/s');

AthroatB=Athroat1(1)
figure(6)
 %plot (time,reg(:,1),'b');
 %hold on
 plot (time,reg(:,2),'b+');
 hold on
 %plot(time,reggin,'r');
 %hold on
 xlabel('time, s')
 ylabel('regression rate, in/s')

 figure(7)
 plot(xloc, h, 'r')
 xlabel('axial location, in   throat @x=xthroat')
 ylabel('h, but/in2-s-R')
 hold on
 plot(xthroat, h, 'bla');
 hold on
 figure(8)
 plot(xloc,q,'r')
 hold on
 ylabel('q, but/in2-s')
 xlabel('axial location, in   throat @ x=xthroat')
 plot(xthroat, q,'bla')
 hold on
 figure(9)
 plot(xloc,M)
 ylabel('Mach')
 hold on
 plot(xloc,rloc)
toc
Averages =

  1.0e+003 *

  Column 1
```

```
    0.009965398394511

  Column 2

    0.071300935367459

  Column 3

    4.041180000000001

  Column 4

    0.051953185446713


ofrange =

  Column 1

    8.486942336716755

  Column 2

    8.448627249161108

Warning: Ignoring
extra legend
entries.
Warning: Ignoring
extra legend
entries.
Warning: Ignoring
extra legend
entries.
Warning: Ignoring
extra legend
entries.
Warning: Ignoring
extra legend
entries.

AthroatB =

    0.303857983047858

Elapsed time is 19.847197 seconds.
```

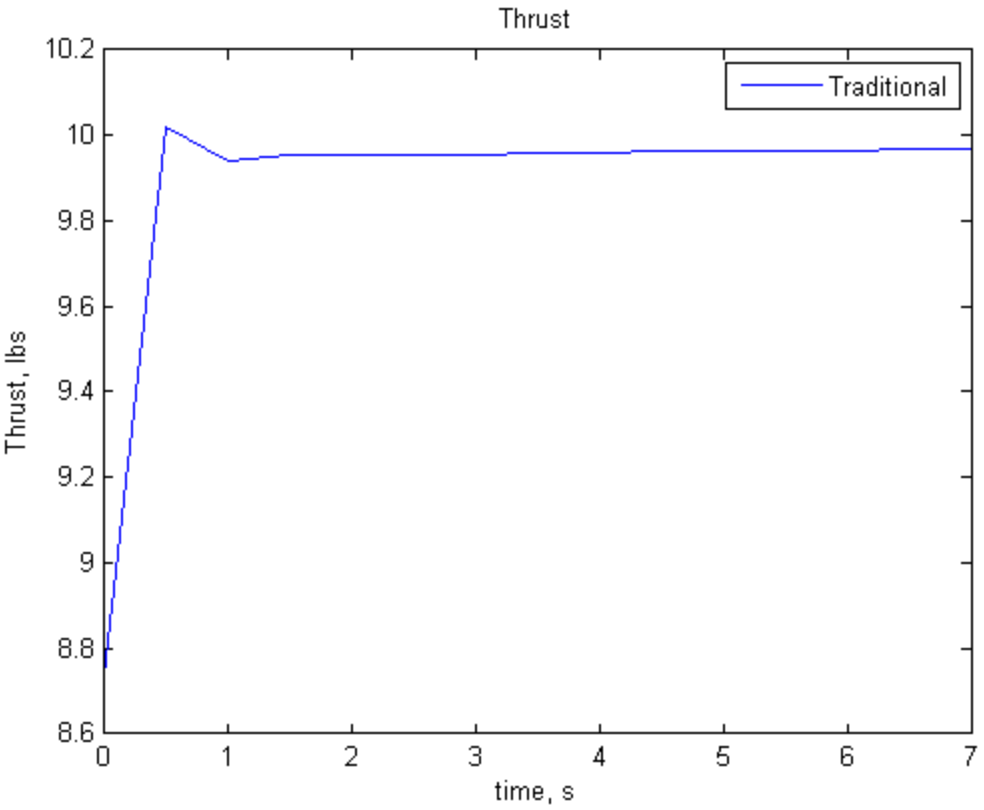
Thrust
Traditional
Thrust, lbs
time, s
10.2
10
9.8
9.6
9.4
9.2
9
8.8
8.6
0
1
2
3
4
5
6
7

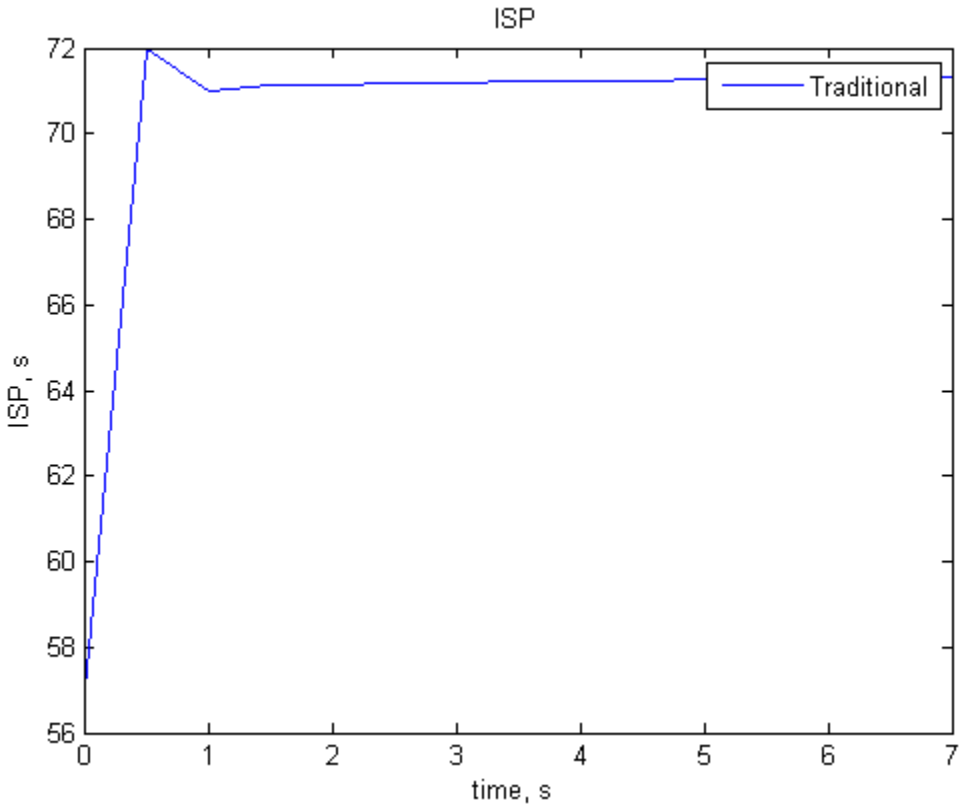
ISP
Traditional
ISP, s
time, s
72
70
68
66
64
62
60
58
56
0
1
2
3
4
5
6
7

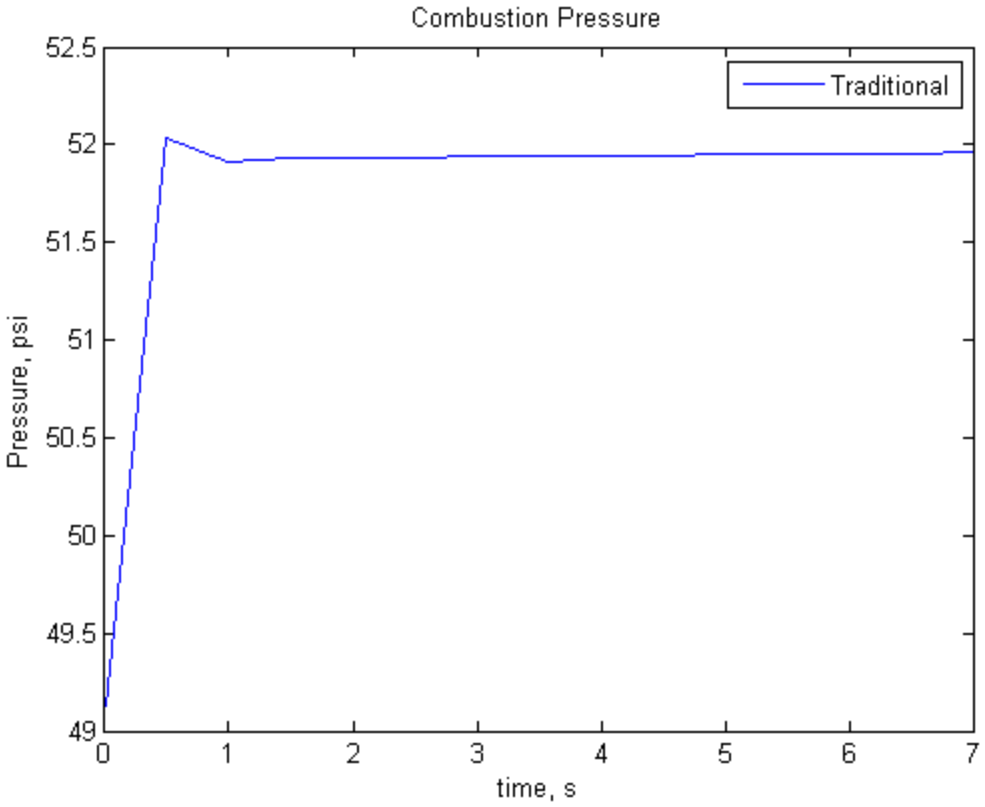
Combustion Pressure
Traditional
Pressure, psi
time, s
52.5
52
51.5
51
50.5
50
49.5
49
0
1
2
3
4
5
6
7

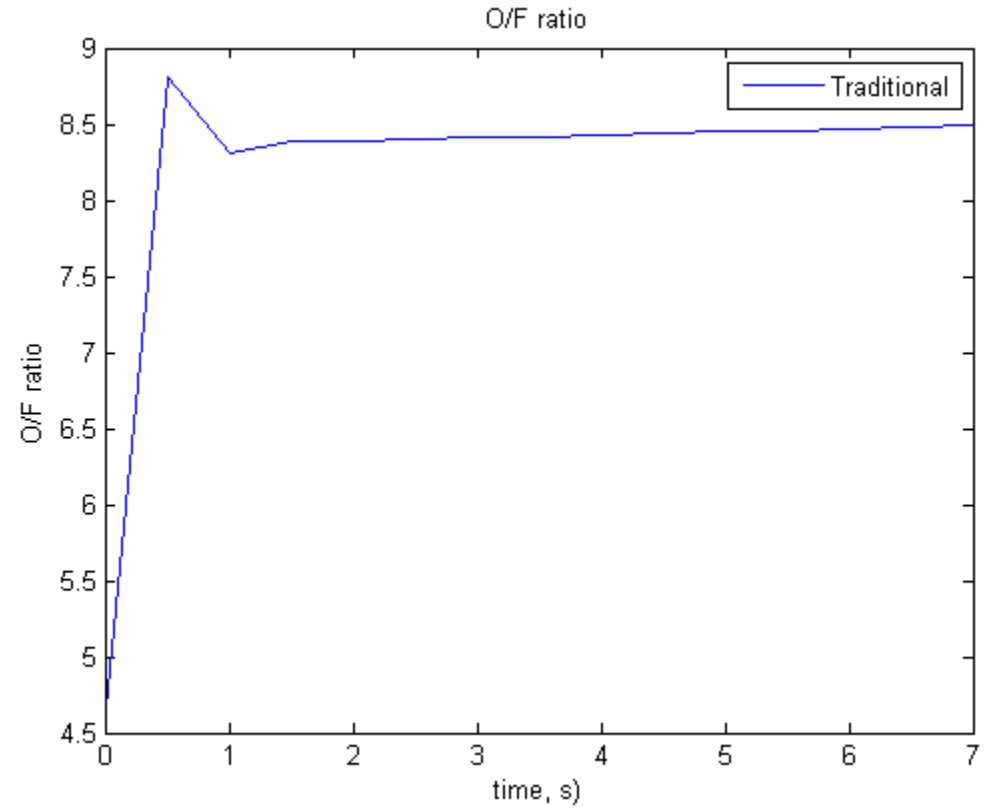
O/F ratio
Traditional
O/F ratio
time, s)
9
8.5
8
7.5
7
6.5
6
5.5
5
4.5
0
1
2
3
4
5
6
7

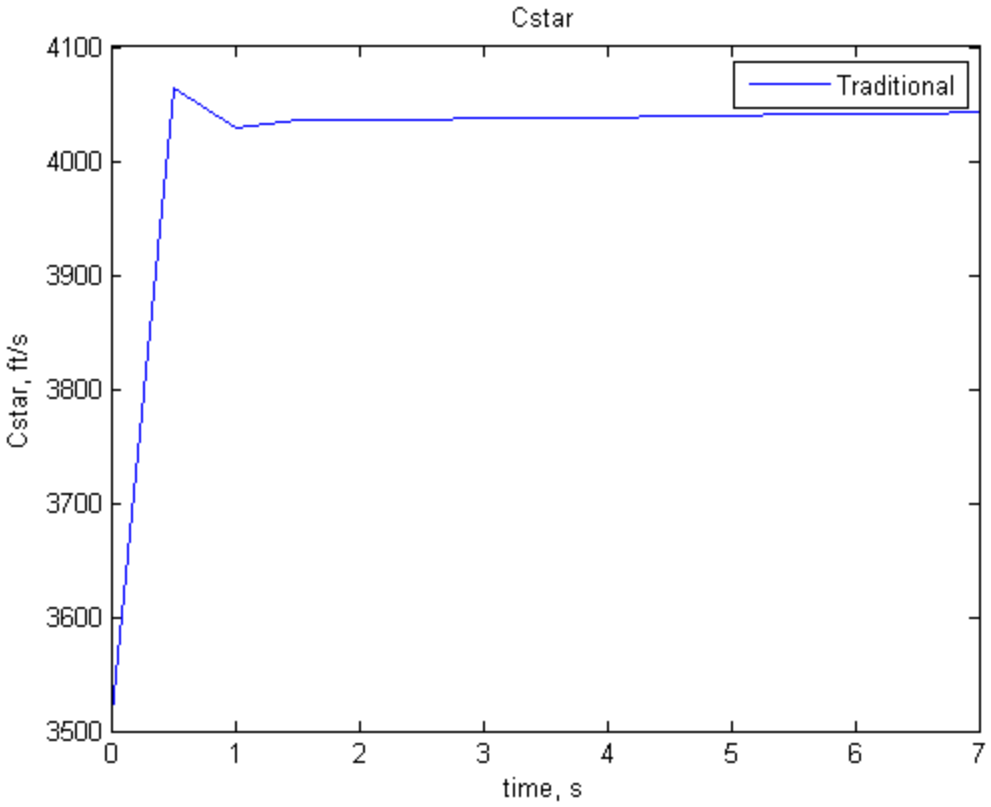
Cstar
Traditional
Cstar, ft/s
time, s
4100
4000
3900
3800
3700
3600
3500
0
1
2
3
4
5
6
7

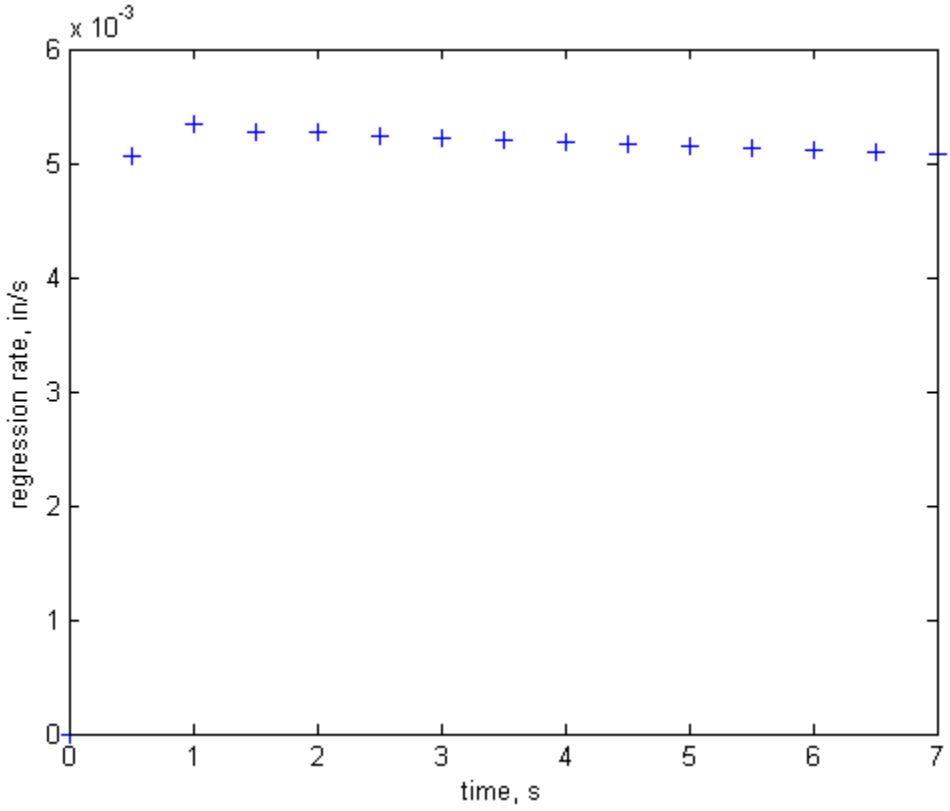
x 10^-3
regression rate, in/s
time, s
6
5
4
3
2
1
0
0
1
2
3
4
5
6
7

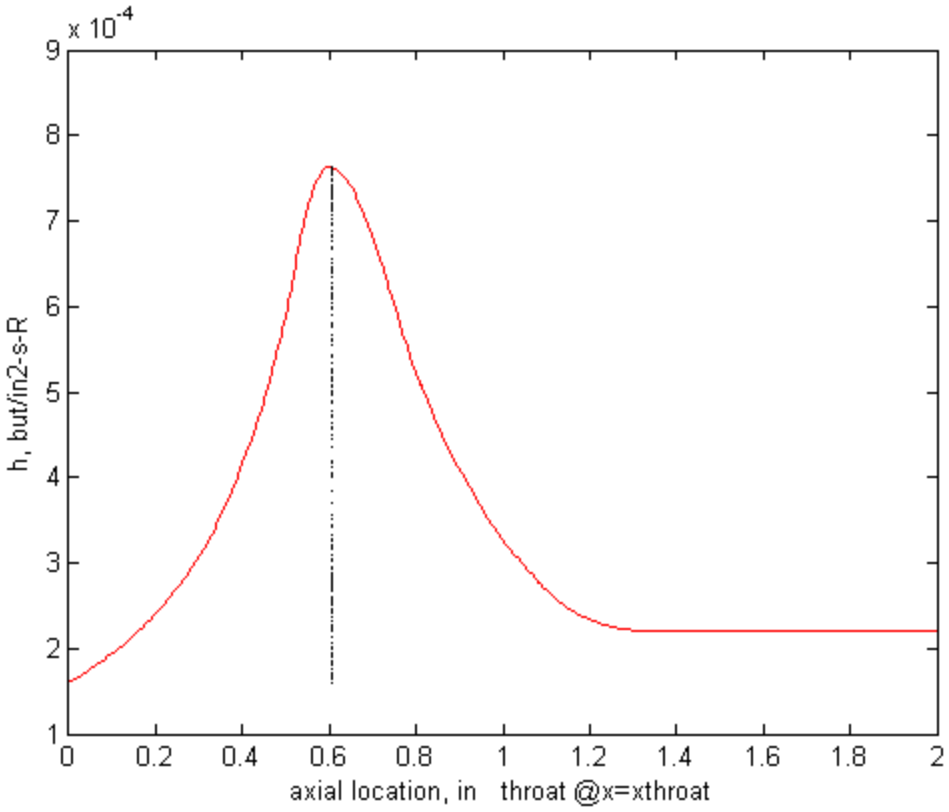
x 10^-4
h, but/in2-s-R
axial location, in throat @x=xthroat

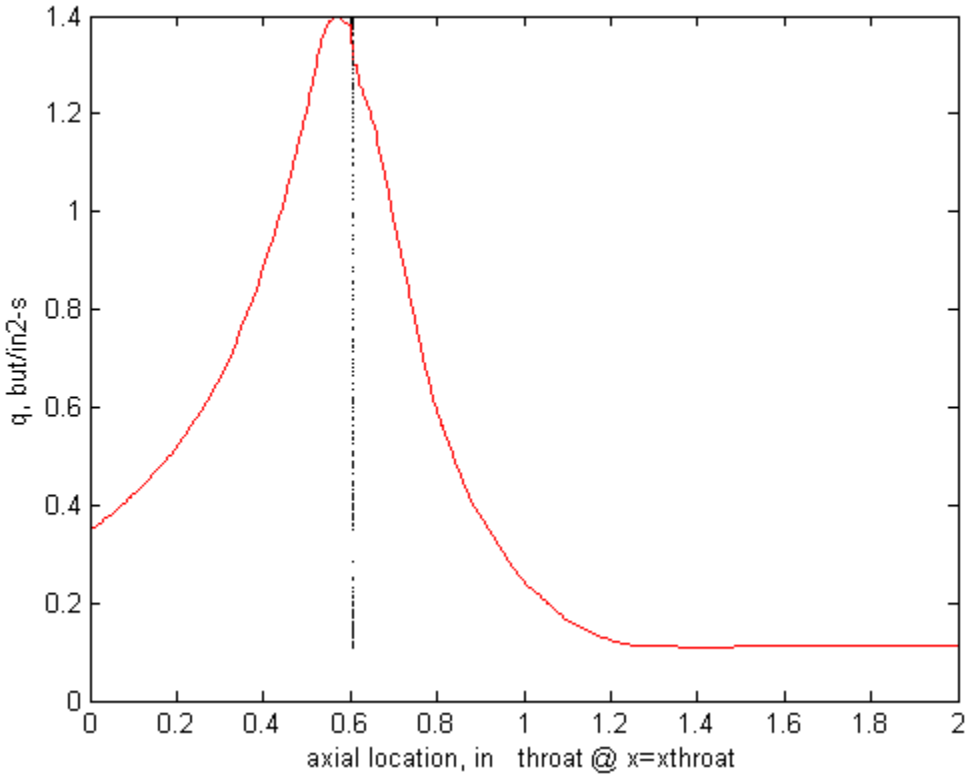
q, but/in2-s
axial location, in throat @ x=xthroat

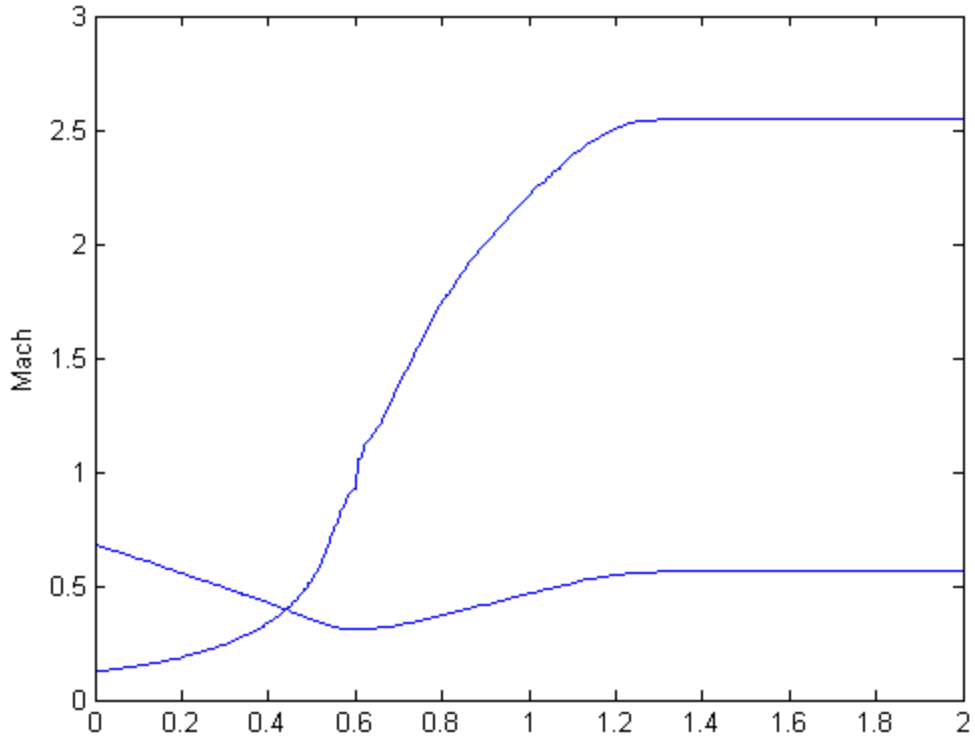

Published with MATLAB® 7.9

Heat Flux function used in performance code

```
function [h, q, rloc, xloc, M, Thg]=nozzleheatflux(rsi, T0, mu, CP, Pr, Pnot,
Cstary, Twh, gamma, omega, radc, nozzle_profile)

rloc=nozzle_profile(:,2);
xloc=nozzle_profile(:,1);
rloc=rloc/12;
xloc=xloc/12;
rsi=rsi/12;
rc=radc/12;
T0=T0*1.8; %K to R
mu=mu*6.72*10^-5; %millipioise to lbm/ft-s
CP=CP*0.2388*4.184;% kcal/kg-k to btu/lbm-R
Pnot=Pnot*144; %psi to lbf/ft2
%% constants for testing
% clear all
% clc
% nozzle_profile=dlmread('xy_jmax.dat');
% rloc=nozzle_profile(:,2);
% xloc=nozzle_profile(:,1);
% rloc=rloc/12;
% xloc=xloc/12;
```

```
% rsi=0.3/12;
% T0=3300;
% mu=0.986*6.72*10^-5;
% CP=0.9511*0.240;
% Pnot=300*144;
% Cstary=5000;
% Twh=1459;
% gamma=1.1;
% omega=0.68;
% Pr=0.7;
% %xthroat=0.7/12;
% rc=0.1/12; %rc=0.5-1.5 rsi

%%
dstar=2*(rsi);
astar=pi()*(rsi)^2;
n=length(rloc);
i=1;
%defining initial guess for subsonic and supersonic solutions
for i=1:n;
    area(i)=pi()*(rloc(i))^2;
    alpha(i)=area(i)/astar;
end
    for i=1:117
        Mo(i)=.2;
    end
    for i=118:n
            Mo(i)=2;
    end


% newton's method
b=(gamma+1)/(2*gamma-2);
c=2/(gamma+1);
n;
Mo;
ft=1;
for ft=1:n
%     if ft==118
%         M(ft)=1
%         e=0.0001;
%     else
%         e=1;
%     end
e=1;
Mit=Mo(ft);
while e>0.09
fm=alpha(ft)*Mit-c^(b)*(1+(Mit^2)/(2*b*c))^b;
dfm=alpha(ft)-c^(b-1)*Mit*(1+(Mit^2)/(2*b*c))^(b-1);
Mnit=Mit-fm/dfm;
e=abs(Mnit-Mit);
Mit=Mnit;
M(ft)=Mit;
end
ft=ft+1;
end
```

```
Tog=T0;
%finding heat transfer coefficient and heat flux
for toy=1:n;
h(toy)=0.026*(1/144)/(dstar^0.2)*(mu^(0.2)*CP/(Pr^0.6))*(Pnot*32.2/Cstary)^(0
.8)*(dstar/rc)^(0.1)*(astar/area(toy))*[1/(0.5*(Twh/Tog)*(1+(M(toy)^2)*(gamma
-1)/2)+0.5)^(0.8-0.2*omega)*(1+M(toy)^2*(gamma-1)/2)^(0.2*omega)];
Thg(toy)=Tog/(1+0.5*(gamma-1)*(M(toy)^2));
q(toy)=h(toy)*(Thg(toy)-Twh);
end


% figure(1)
% plot(xloc, q)
% ylabel('q, btu/in2-s')
% hold on
% figure(2)
% plot(xloc,h);
% ylabel('h, btu/in2-s-R')
% figure(3)
% plot(xloc,rloc);
% ylabel('radius, ft')
% hold on
% figure(4)
% plot(xloc,M);
```

MATLAB DAQ Code

```
%% DAQ setup for the cooled rocket inputs: force, pressure, temperature,gas
%% flow and water flow
%% Channel Settings
    %0-Pressure
    %1-Ox Flow
    %2-Froce Transducer

clear all
clc

% recognize the board
% to find out the ID type: daqwinfo('mcc')

Minilab=analoginput('mcc','0');

%TCb=analoginput('mcc','1');
%%
%add channels
addchannel(Minilab,0:3);
%addchannel(TCb,0:6);

% getdata - extract analog input data, time, and event information from data
aquaition engine
% peekdata  preview most recent acquired analog input data

% set the sampling rate to 20 hz and aquir 6000 samples, (5min)
set(Minilab,'SampleRate',100); %100 - 2000 for minilab
```

```
set(Minilab,'SamplesPerTrigger',18000);



% acquire data
tic
start(Minilab);
%start(TCb);
wait(Minilab,180)%300 seconds maximum wait time
toc
%wait(TCb);
data=getdata(Minilab);
%data1=getdata(TCb);
dlmwrite('2_18_14_Test4.txt',data,' ')
plot(data);
delete(Minilab);
clear Minilab;   %gets rid of Minilab acquired data

%% treating the counter as a pulse  and create a plot of rising times to
% %% create a totalizer
%
% % Counting pulses
%
% % Set the threshold to 3.5 V.
% threshold = 3.5;
%
% % Create the offset data.  Need to append a NaN to the final sample since
% % both vectors need to have the same length.
% offsetData = [data(2:end); NaN];
%
% % Find the rising edge.
% risingEdge = find(data < threshold & offsetData > threshold);
%
%
% % Show the rising edges with red x's.
% hold on
% plot(time(risingEdge), threshold, 'rx');
%
% % Show the falling edges with green o's.
% plot(time(fallingEdge), threshold, 'go');
% hold off
%
% % Construct a vector to hold all of the times.
% pulseIndices = zeros(length(risingEdge), 1);
%
% % Store the rising edge times.
% pulseIndices(1:2:end) = risingEdge;
```

Minimum wall thickness Calculation for Inconel 625

Table 14 Values used for minimum wall thickness calculation

Max shear stress @ 1200 F, ksi	Factor of Safety	Pressure, psi	Channel Width, in
82	2	600	0.03

$$82000 * w_t = 600 * 0.03 * 2$$
$$w_t = 4.39x10^{-4} \text{ inches}$$

Sample Calculation of water flow velocity through the nozzle channels.

Table 15 Values for Sample calculation of Water Flow velocity through the nozzle

Density, lbm/ft^3	Area per channel, ft^2	Number of channels	Target flow rate, lbm/s
62.3	2.11x10^{-5}	48	2.5

$$\dot{m} = \rho V A \rightarrow V = {\dot{m}}/{\rho * A}$$
$$V = {2.5}/{62.3 * 2.11E - 5} = 39.62 \text{ ft/s}$$

VITA

John Nicholas Quigley was born in July of 1988 and raised between Memphis, TN and Lexington, KY before he came to Knoxville, TN to study Aerospace Engineering at the University of Tennessee. He has enjoyed many successes and learned from various failures. He has been very fortunate to have the opportunity to carry out the work presented in this thesis with the assistance and under the tutelage of many very intelligent and helpful people.